Nucleon isovector couplings in $N_f = 2+1$ lattice QCD at the physical point

Ryutaro Tsuji[1,2,*] Natsuki Tsukamoto,[1] Yasumichi Aoki,[2] Ken-Ichi Ishikawa,[3] Yoshinobu Kuramashi,[4]
Shoichi Sasaki,[1,†] Eigo Shintani,[4] and Takeshi Yamazaki[5,4]

(PACS Collaboration)

[1]*Department of Physics, Tohoku University, Sendai 980-8578, Japan*
[2]*RIKEN Center for Computational Science, Kobe 650-0047, Japan*
[3]*Core of Research for the Energetic Universe, Graduate School of Advanced Science and Engineering,*
Hiroshima University, Higashi-Hiroshima 739-8526, Japan
[4]*Center for Computational Sciences, University of Tsukuba, Tsukuba, Ibaraki 305-8577, Japan*
[5]*Faculty of Pure and Applied Sciences, University of Tsukuba, Tsukuba, Ibaraki 305-8571, Japan*

We present results for the scalar and tensor isovector-couplings (g_S and g_T) of the nucleon measured at the physical point ($M_\pi = 135$ MeV) with a single lattice spacing of 0.085 fm in $2+1$ flavor QCD. Our calculations are carried out with two ensembles of gauge configurations generated by the PACS Collaboration with nonperturbatively $\mathcal{O}(a)$ improved Wilson quark action and Iwasaki gauge action on $(10.9 \text{ fm})^4$ and $(5.5 \text{ fm})^4$ lattices, where the finite-size effect on the nucleon mass was not shown at the level of statistical precision less than 0.5%. We compute the nucleon three-point correlation functions in the vector, axial, scalar, and tensor channels. We confirm that our previous result of the nucleon axial coupling on the large spatial volume of $(10.9 \text{ fm})^4$ has no finite-size effect at the level of the statistical precision of 1.9%. For the renormalization, we first renormalize g_S and g_T nonperturbatively using the RI/SMOM$_{(\gamma_\mu)}$ scheme, a variant of Rome-Southampton RI/MOM scheme with reduced systematic errors, as the intermediate scheme. We evaluate our final results at the renormalization scale of 2 GeV in the $\overline{\text{MS}}$ scheme through the matching procedure between the RI/SMOM$_{(\gamma_\mu)}$ and $\overline{\text{MS}}$ schemes with the help of perturbation theory, and then obtain $g_S = 0.927(83)_{\text{stat}}(22)_{\text{syst}}$ and $g_T = 1.036(6)_{\text{stat}}(20)_{\text{syst}}$.

I. INTRODUCTION

Future and current precision β-decay measurements with cold and ultracold neutrons provide us an opportunity to study the sensitivity of the nucleon isovector matrix elements to new physics beyond the standard model (BSM) [1]. The neutron lifetime puzzle associated with the nucleon axial-vector coupling (g_A) is one of such examples. The discrepancy between the results of beam experiments and storage experiments remains unsolved. It is still an open question that deserves further investigation in terms of the ratio of the nucleon axial and vector couplings (g_A/g_V) [2]. Although the vector and axial-vector channels dominate the weak decay of the neutron, there is no reason to forbid the other channel contributions to the neutron decay if the BSM contributions are present. Therefore, the scalar, pseudoscalar and tensor contributions, whose couplings are less known experimentally, play important roles to constrain the limit of nonstandard interactions mediated by undiscovered gauge bosons in the scalar, pseudoscalar and tensor channels [3–5].

In general the isovector nucleon couplings g_O for $O = V$ (vector), A (axial-vector), S (scalar), P (pseudoscalar), and T (tensor) are expressed by the neutron-proton transition matrix element with quark charged (off-diagonal) currents

$$\langle p(p,s)|\bar{u}\Gamma^O d|n(p,s)\rangle = g_O \bar{u}_p(p,s)\Gamma^O u_n(p,s), \quad (1)$$

where Γ^O is a Dirac matrix appropriate for the channel O ($O = V, A, S, P, T$). Considering the $SU(2)$ Lie algebra associated with isospin, the isovector nucleon matrix elements can be rewritten by the proton matrix elements of the diagonal isospin current

[*]tsuji@nucl.phys.tohoku.ac.jp
[†]ssasaki@nucl.phys.tohoku.ac.jp

$$\langle p|\bar{u}\Gamma^O d|n\rangle = \langle p|\bar{u}\Gamma^O u|p\rangle - \langle p|\bar{d}\Gamma^O d|p\rangle \qquad (2)$$

in the isospin limit. Therefore, the isovector couplings are related to the isovector charges of the proton and they are rewritten by

$$g_O = g_O^u - g_O^d, \qquad (3)$$

where up and down quark contributions of the proton's isovector-charges g_O^u and g_O^d are defined by the proton forward matrix elements as $g_O^f = \langle p(p,s)|\bar{f}\Gamma^O f|p(p,s)\rangle$ with $f = u$ or d. Recall that for the vector $g_V = 1$ is satisfied under the exact isospin symmetry.

The nucleon scalar isovector-coupling g_S, which is related to the size of the neutron-proton mass splitting induced solely by the light-quark mass difference in the absence of electromagnetic effects, is a phenomenologically interesting quantity [6]. On the other hand, each flavor contribution of the proton's tensor charges g_T^f is a weight factor for the contributions of the nonvanishing quark electric dipole moment (EDM) to the proton and neutron EDMs, since the tensor current has the same transformation properties under P and T discrete symmetries as the EDM current [7,8]. Furthermore, the nucleon tensor isovector-coupling g_T itself is also an important information from the viewpoint of the proton spin structure [9]. The proton's tensor-charge is closely connected with the first Mellin moment of the proton's transversity parton distribution function (PDF), which has been recently studied in experiments such as semi-inclusive deeply inelastic scattering (SIDIS) and Drell-Yan measurements from HERMES at DESY, COMPASS at CERN and SoLID at Jefferson Lab. Recently, the first global analysis of the quark transversity distributions with the available SIDIS data under the constraint of lattice estimates of g_T has demonstrated significant reduction of the uncertainties on the resulting transversity PDFs [10].

As described previously, the knowledge of the nucleon scalar and tensor isovector-couplings is necessary for ongoing experimental researches for the BSM physics and also for the nucleon structure. Although the vector and axial-vector isovector-couplings (g_V and g_A) are well measured in both experiment and lattice QCD, the scalar and tensor isovector-couplings (g_S and g_T) are so far not accessible in experiment. Of course, since the precise experiments are not yet available for g_S and g_T, their accurate determination from lattice QCD is highly desired. Lattice determinations of g_S and g_T have recently been performed by several groups [11–20]. As shown in FLAG Review [11], the most precise determination of g_S and g_T is given by a single group (PNDME Collaboration) [14,15] and their values are dominant in the FLAG average for $N_f = 2 + 1 + 1$. Their calculation had been performed with the mixed action simulations using the Wilson-clover valence quarks on the asqtad-improved gauge

configurations with the highly improved staggered sea quarks (HISQ). This implies that their lattice QCD simulations are *not* fully dynamical ones, but rather *partially quenched* ones since they used the different action for the sea and valence quarks. Even if we could not overcome the current precision given by the PNDME Collaboration, it is worth to reproduce their results in *fully dynamical lattice QCD simulations*. Further comprehensive studies of the nucleon isovector-couplings including g_S and g_T as well as g_V and g_A are still needed. In this study, we intend to determine g_A, g_S, and g_T with high accuracy and high precision using the $2 + 1$ flavor lattice QCD at the physical point on sufficiently large volume.

This paper is organized as follows. In Sec. II, we describe our method to calculate the nucleon isovector-couplings from the nucleon 2- and 3-point correlation functions in lattice simulations. In Sec. III, we give a short outline of the renormalization procedure with the RI/SMOM and RI/SMOM$_{\gamma_\mu}$ intermediate schemes to connect the bare lattice operators to the continuum renormalized operators. The simulation parameters are described in Sec. IV. We also explain the error reduction technique employed in this study. The results of our lattice calculations for the nucleon isovector-couplings are presented in Sec. V, which is divided into three subsections. We first determine the bare values of the nucleon isovector-couplings for the vector, axial-vector, scalar, and tensor channels in Sec. V A. Section V B presents the results of the renormalization constants for the scalar and tensor. The results of the renormalized couplings are presented in the last subsection (Sec. V C). Finally, we close with summary in Sec. VI. All dimensionful quantities are expressed in units of the lattice spacing throughout this paper, unless otherwise explicitly specified. A bold-faced variable represents a three-dimensional vector.

II. CALCULATION METHOD I: BARE COUPLING

In this section we describe our method to calculate the nucleon isovector-couplings from the nucleon 2- and 3-point correlation functions, which consist of the nucleon source and sink interpolating operators (denoted as $\bar{N}(x)$ and $N(x)$, respectively), and the quark bilinear current operator $J(x)$.

A. Nucleon 2-point correlation function

In this study, two types of smeared quark operator $q_S(t, \mathbf{x})$ are used for the construction of the nucleon interpolating operator as well as a local quark operator $q(t, \mathbf{x})$. The smeared quark operator is given by a convolution of the local quark operator with a smearing function $\phi(\mathbf{x}, \mathbf{y})$ as

$$q_S(t, \mathbf{x}) = \sum_{\mathbf{y}} \phi(\mathbf{x}, \mathbf{y}) q(t, \mathbf{y}), \qquad (4)$$

where the color and Dirac indices are omitted.

In the case of the exponentially smeared quark operator, a smearing function $\phi(\mathbf{x}, \mathbf{y})$ is given by an isotropic function of $r = |\mathbf{x} - \mathbf{y}|$ in a linear spatial extent of L as the following form

$$\phi(\mathbf{x}, \mathbf{y}) = \phi(r) = \begin{cases} 1 & (r = 0) \\ Ae^{-Br} & (r < L/2) \\ 0 & (r \geq L/2) \end{cases} \quad (5)$$

with two smearing parameters A and B. This procedure does not preserve the full gauge invariance of the hadron 2-point correlation functions consisting of the spatially smeared quark operators, so that the Coulomb gauge fixing is necessary. We have always adopted the exponentially smeared quark operator as the spatially smeared method for the quark operator in our previous studies [21–23]. In this study, we then adopt it as the primary smeared method in both two volumes ($L = 128$ and $L = 64$). In addition, the other type of the spatially smeared quark operator is also used in the larger volume ($L = 128$) as a supplementary result. For this purpose, we use gauge-covariant, approximately Gaussian-shaped smearing method (denoted shortly as Gaussian smearing) [24].

To maintain the gauge covariance of the smeared quark operator through Eq. (4), we construct the following smearing function:

$$\phi(\mathbf{x}, \mathbf{y}) \to \phi(\mathbf{x}, \mathbf{y}; U) = \delta_{\mathbf{x}, \mathbf{y}} + \frac{w_G^2}{4n_G} \boldsymbol{\Delta}(\mathbf{x}, \mathbf{y}; U), \quad (6)$$

where n_G and w_G represent two smearing parameters.[1] Here, $\boldsymbol{\Delta}(\mathbf{x}, \mathbf{y}; U)$ represents the three-dimensional covariant Laplacian, which is defined with the spatial components of the link variables $U_\mu(x)$ ($\mu = 1, 2, 3$)[2] as

$$\boldsymbol{\Delta}(\mathbf{x}, \mathbf{y}; U) = \sum_{\mu=1}^{3} [U_\mu(x)\delta_{\mathbf{x}+\hat{\mu}, \mathbf{y}} + U_\mu^\dagger(x - \hat{\mu})\delta_{\mathbf{x}-\hat{\mu}, \mathbf{y}} - 2\delta_{\mathbf{x}, \mathbf{y}}],$$

$$(7)$$

which ensures that the gauge covariance of the spatially extended quark operator is preserved. Applying the same

---

[1]In Ref. [24], the smearing function is chosen as

$$\phi(\mathbf{x}, \mathbf{y}; U) = \delta_{\mathbf{x}, \mathbf{y}} + \alpha \sum_{\mu=1}^{3} [U_\mu(x)\delta_{\mathbf{x}+\hat{\mu}, \mathbf{y}} + U_\mu^\dagger(x - \hat{\mu})\delta_{\mathbf{x}-\hat{\mu}, \mathbf{y}}].$$

The parameter α that corresponds to the coupling strength of the nearest neighbors is related with our parameter set of (n_G, w_G) as $\alpha = \frac{w_G^2/4n_G}{1 - 3w_G^2/2n_G}$. The positivity of α requires the condition of $3w_G^2 < 2n_G$ in our parameter set.

[2]In this study, six steps of stout-smearing are applied to the link variables.

procedure recursively, an approximately Gaussian-shaped quark operator can be obtained through this iterative scheme. When the number of the iteration is chosen to be n_G, w_G corresponds to the width of the Gaussian that results in $n_G \to \infty$.

The nucleon 2-point function with the local nucleon sink operator $N_L(t, \mathbf{x})$ and smeared nucleon source operator $\bar{N}_S(t, \mathbf{x})$ is defined as

$$C_{2\mathrm{pt}}^{LS}(t - t_{\mathrm{src}}, \mathbf{x} - \mathbf{x}_{\mathrm{src}}) = \frac{1}{4}\mathrm{Tr}[\mathcal{P}_+ \langle 0|N_L(t, \mathbf{x})\bar{N}_S(t_{\mathrm{src}}, \mathbf{x}_{\mathrm{src}})|0\rangle],$$

$$(8)$$

where $\mathcal{P}_+ = (1 + \gamma_4)/2$,[3] and the nucleon operator is given for the proton state by

$$N_L(t, \mathbf{x}) = \epsilon_{abc} u_a^T(t, \mathbf{x}) C\gamma_5 d_b(t, \mathbf{x}) u_c(t, \mathbf{x}) \quad (9)$$

with $C = \gamma_4\gamma_2$, the up and down quark operators u, d and a, b, c being the color indices. The smeared source operator $N_S(t, \mathbf{x})$ is the same as the local one $N_L(t, \mathbf{x})$, but all the quark operators u, d are replaced by the smeared ones defined in Eq. (4). The momentum projected 2-point function is then given by

$$\tilde{C}_{2\mathrm{pt}}^{XS}(t, \mathbf{p}) = \sum_{\mathbf{r}} e^{-i\mathbf{p}\cdot\mathbf{r}} C_{2\mathrm{pt}}^{XS}(t, \mathbf{r}) \quad (10)$$

with $X = L$, S and a three-dimensional momentum $\mathbf{p}$.

B. Nucleon 3-point correlation function

In order to calculate the isovector nucleon matrix element, we evaluate the nucleon 3-point functions, which are constructed with the spatially smeared source and sink operators of the nucleon and a given isovector current operator J^O inserted at $t = t_{\mathrm{op}}$ being subject to a range of $t_{\mathrm{sink}} > t_{\mathrm{op}} > t_{\mathrm{src}}$ as

$$C_O^k(t_{\mathrm{op}} - t_{\mathrm{src}}, \mathbf{x} - \mathbf{x}_{\mathrm{src}})$$
$$= \frac{1}{4}\sum_{\mathbf{y}}\mathrm{Tr}[\mathcal{P}_k \langle 0|N_S(t_{\mathrm{sink}}, \mathbf{y})J^O(t_{\mathrm{op}}, \mathbf{x})\bar{N}_S(t_{\mathrm{src}}, \mathbf{x}_{\mathrm{src}})|0\rangle],$$

$$(11)$$

where $\mathcal{P}_k$ is a projection operator, and J^O is defined by the local bilinear operator as $J^O = \bar{u}\Gamma^O u - \bar{d}\Gamma^O d$ with a Dirac matrix Γ^O appropriate for the channel O ($O = V, A, S, P, T$). The momentum projected 3-point function is then given by

---

[3]A projection operator $\mathcal{P}_+$ can eliminate contributions from opposite-parity state [25,26].

$$\tilde{C}_O^k(t, \mathbf{p}) = \sum_{\mathbf{r}} e^{-i\mathbf{p}\cdot\mathbf{r}} C_O^k(t, \mathbf{r}). \tag{12}$$

A well-known procedure for determining the couplings is to calculate the following ratio of the zero-momentum projected 3- and 2-point functions with a fixed source-sink separation ($t_{\mathrm{sep}} \equiv t_{\mathrm{sink}} - t_{\mathrm{src}}$) as

$$R(t_{\mathrm{op}}, t_{\mathrm{sep}}) \equiv \frac{\tilde{C}_O^k(t_{\mathrm{op}} - t_{\mathrm{src}}, \mathbf{0})}{\tilde{C}_{2\mathrm{pt}}^{SS}(t_{\mathrm{sep}}, \mathbf{0})}, \tag{13}$$

where the nucleon 2-point function is given by the same smeared source and sink operators. If the condition $t_{\mathrm{sep}} \gg t_{\mathrm{op}} - t_{\mathrm{src}} \gg 0$ is satisfied, the desired coupling g_O relevant for the O channel can be read off from an asymptotic plateau of the ratio (hereafter denoted as the plateau method), which is independent of a choice of t_{op} as

$$R(t_{\mathrm{op}}, t_{\mathrm{sep}}) \xrightarrow[t_{\mathrm{sep}} \gg t_{\mathrm{op}} - t_{\mathrm{src}} \gg 0]{} g_O + \mathcal{O}(e^{-\Delta E(t_{\mathrm{op}} - t_{\mathrm{src}})})$$
$$+ \mathcal{O}(e^{-\Delta E(t_{\mathrm{sep}} - t_{\mathrm{op}} + t_{\mathrm{src}})}), \tag{14}$$

where $\Delta E = E_1 - E_0$ denotes a difference between the two energies of the ground state (E_0) and the lowest excited state (E_1). Narrower source-sink separation causes systematic uncertainties stemming from the excited-state contamination represented by two terms of $\mathcal{O}(e^{-\Delta E(t_{\mathrm{op}} - t_{\mathrm{src}})})$ and $\mathcal{O}(e^{-\Delta E(t_{\mathrm{sep}} - t_{\mathrm{op}} + t_{\mathrm{src}})})$. The optimal choice of the smearing parameters can help to suppress as much as possible the coefficients of these terms due to the maximal overlap with the ground state.

Here, recall that the ratio vanishes unless $\Gamma^O = 1(S)$, $\gamma_4(V)$, $\gamma_i\gamma_5(A)$, and $\sigma_{ij}(T)$ with $i, j = 1, 2, 3$ [27]. The projection operator $\mathcal{P}_k$ ($k = t, 5x, 5y, 5z$) is supposed to be chosen as below

$$\mathcal{P}_k = \begin{cases} \mathcal{P}_{+\gamma_5\gamma_1}(k=5x) & \text{for } \Gamma^O = \gamma_5\gamma_1(A), \quad \sigma_{23}(T) \\ \mathcal{P}_{+\gamma_5\gamma_2}(k=5y) & \text{for } \Gamma^O = \gamma_5\gamma_2(A), \quad \sigma_{31}(T) \\ \mathcal{P}_{+\gamma_5\gamma_3}(k=5z) & \text{for } \Gamma^O = \gamma_5\gamma_3(A), \quad \sigma_{12}(T) \\ \mathcal{P}_{+\gamma_4}(k=t) & \text{for } \Gamma^O = 1(S), \quad \gamma_4(V). \end{cases} \tag{15}$$

In this study we focus on the axial (A), scalar (S), and tensor (T) channels.

In general, the nucleon 3-point functions have the connected and disconnected contributions, which correspond to the two types of Wick contraction topologies for all quark lines. The disconnected contributions corresponding to the sea quark effect are necessary for determining flavor diagonal charges of the nucleon, g_O^q ($q = u, d, s, \cdots$). However, a computation of disconnected diagrams requires much-higher computational cost than that of connected diagrams. Recalled that in the case of $2 + 1$ flavor lattice QCD, where the up and down quark

masses are equal, the nucleon 3-point functions for the isovector current does not receive any contribution from the disconnected-type diagrams since they are canceled each other thanks to the exact isospin symmetry. Therefore, the isovector couplings $g_O = g_O^u - g_O^d$ can be determined only by the connected-type diagrams.

III. CALCULATION METHOD II: RENORMALIZATION

The general idea for the nonperturbative renormalization of the quark operator is discussed in Ref. [28]. Here, we briefly review the Rome-Southampton method [28]. In this paper, we will calculate the renormalization constants for the quark bilinear operators

$$(\bar{q}\Gamma^O q)_R = Z_O(\bar{q}\Gamma^O q)_B, \tag{16}$$

where Γ^O denotes a Dirac gamma matrix appropriate for the channel O ($O = V, A, S, P, T$). The subscripts R and B represent "renormalized" and "bare" operators, respectively. Although we simply note q and $\bar{q}$ for quark and antiquark fields, only flavor nonsinglet operators are considered.

In order to evaluate the renormalization constants Z_O, let us first define the one-side Fourier-transformed quark propagator as

$$S(p|x_0) = \sum_{x'} e^{-ip\cdot x'} S(x', x_0), \tag{17}$$

where $S(x', x_0)$ represents a point-source quark propagator with a fixed source point x_0 in the Landau gauge. The two-point Green's functions with the insertion of the quark bilinear operator $\bar{q}\Gamma^O q$ are given by

$$\langle G_O(p_1, p_2) \rangle = \frac{1}{n_{\mathrm{src}}} \sum_{x_0} \langle S(p_1|x_0) \Gamma^O \gamma_5 S(p_2|x_0)^\dagger \gamma_5 \rangle, \tag{18}$$

where two external quark lines carry momenta p_1 and p_2. Here, recall that the explicit dependence of source location x_0 is averaged over finite number of different source locations (n_{src}). In this study, $n_{\mathrm{src}} = 4$ is chosen.

We then compute the bare vertex function (or amputated Green's function) as

$$\Lambda_O(p_1, p_2) = \left[\frac{1}{n_{\mathrm{src}}} \sum_{x_0} \langle S(p_1|x_0) \rangle\right]^{-1} \langle G_O(p_1, p_2) \rangle$$
$$\times \left[\frac{1}{n_{\mathrm{src}}} \sum_{x_0} \langle \gamma_5 S(p_2|x_0)^\dagger \gamma_5 \rangle\right]^{-1}. \tag{19}$$

Following Ref. [28], we define the renormalized vertex function by

$$(\Lambda_O)_R = \frac{Z_O}{Z_q}(\Lambda_O)_B, \qquad (20)$$

where Z_q denotes the quark field renormalization constant.

In the regularization independent (RI) momentum-subtraction scheme, the Z factors are fixed by imposing the following renormalization condition

$$(\Lambda_O)_R|_{\mu^2=\mu^2(p_1,p_2)} = (\Lambda_O)_{\text{tree}} = \Gamma^O, \qquad (21)$$

where the renormalization scale μ is introduced according to the subtraction kinematics with the external quark momenta p_1 and p_2. In practice, the ratio of the renormalization constants Z_O/Z_q is calculated from the projected vertex functions with the appropriate projection operator $\mathcal{P}_O$:

$$\frac{Z_O}{Z_q}\text{Tr}[(\Lambda_O)_B\mathcal{P}_O]\bigg|_{\mu^2=\mu^2(p_1,p_2)} = \text{Tr}[\Gamma^O\mathcal{P}_O], \qquad (22)$$

where the symbol "Tr" means a trace over color and Dirac indices. There is no unique choice of the projection operators and the momentum subtraction kinematics. There are some variants of the RI schemes as enumerated later in Sec. III A.

Although the field renormalization constant Z_q can be solely evaluated, the value of Z_O given by taking the product of Z_O/Z_q with Z_q is strongly affected by statistical fluctuations on Z_q. Recall that Z_V and Z_A are precisely determined using the Schrödinger functional (SF) scheme [29] being independent of the renormalization scheme and scale. Therefore, we simply calculate the ratio of Z_O/Z_q and Z_V/Z_q (or Z_A/Z_q) in the RI scheme without the direct evaluation of Z_q for the scalar and tensor channels ($O = S$ and T). The values of Z_S^{RI} and Z_T^{RI} at a renormalization scale μ can be obtained with help of Z_V^{SF} or Z_A^{SF} in fully nonperturbative manner. For instance, in the scalar case with Z_V^{SF}, Z_S^{RI} is evaluated by

$$Z_S^{\text{RI}}(\mu^2) = Z_V^{\text{SF}} \times \frac{\text{Tr}[\Gamma_S\mathcal{P}_S]}{\text{Tr}[\Gamma_V\mathcal{P}_V]} \cdot \frac{\text{Tr}[(\Lambda_V)_B\mathcal{P}_V]|_{\mu^2=\mu^2(p_1,p_2)}}{\text{Tr}[(\Lambda_S)_B\mathcal{P}_S]|_{\mu^2=\mu^2(p_1,p_2)}}, \quad (23)$$

where the renormalization scale is introduced by the external momenta p_1 and p_2 as $\mu = \sqrt{p_1^2} = \sqrt{p_2^2}$.

A. Variants of the RI schemes

1. Momentum subtraction (MOM) scheme

The regularization independent momentum-subtraction (RI/MOM) scheme is an intuitive and conventional approach to impose the renormalization condition with a specific kinematics where incoming and outgoing momenta are equal as $p_1 = p_2$. In this kinematics, the projection operator $\mathcal{P}_O$ should be simply chosen to be equal to Γ^O,

since the momentum inserted at the operator becomes zero as $q = p_1 - p_2 = 0$. However, as discussed in Refs. [30,31], the vanishing momentum q enhances unwanted infrared effects such as the chiral symmetry breaking, which causes some large residual scale dependence in the infrared region of the renormalization scale μ. This, indeed, is a major source of systematic uncertainties when the renormalization constants, especially Z_S and Z_P, are determined in the RI/MOM scheme.

2. Symmetric momentum (SMOM) scheme

To avoid the unwanted infrared effects, one may choose the symmetrical momentum configurations $p_1^2 = p_2^2 = q^2$ (denoted as the symmetric momentum (SMOM) scheme). In the RI/SMOM scheme [32], we can expect better infrared behavior than the conventional RI/MOM scheme owing to $q^2 \neq 0$. The use of the nonexceptional momentum configuration, like the symmetric configuration, and its effect to suppress the unwanted infrared effects has first discussed in Ref. [31].

The projection operators can be chosen as below [32].

$$\mathcal{P}_O = \begin{cases} \frac{q^\nu\gamma_\nu q_\mu}{q^2} & \text{for } \Gamma^O = \gamma_\mu \\ \frac{q^\nu\gamma_\nu q_\mu\gamma_5}{q^2} & \text{for } \Gamma^O = \gamma_\mu\gamma_5 \\ 1 & \text{for } \Gamma^O = 1 \\ \gamma_5 & \text{for } \Gamma^O = \gamma_5 \\ \gamma_\mu\gamma_\nu & \text{for } \Gamma^O = \gamma_\mu\gamma_\nu, \end{cases} \qquad (24)$$

where the vector and axial-vector cases can take the projection operators that are different from those used in the RI/MOM scheme, since they can maintain the Ward-Takahashi identities for the vector and axial-vector channels even for finite q.

There is one alternative scheme called the RI/SMOM$_{\gamma_\mu}$ scheme [32], where the projection operators are the same as in the RI/MOM scheme, while the symmetrical momentum configurations are adopted as in the RI/SMOM scheme. The same effect on the suppression of the infrared effects as the RI/SMOM scheme is expected for this scheme as well. Adding another scheme will appear useful to assess the systematic uncertainty associated with the use of the perturbation theory, as different schemes may develop different convergence properties in the perturbative series.

The kinematics of momentum subtraction point and the choice of the projection operators for all three RI schemes are summarized in the Table I.

3. Conversion and evolution

In order to relate operators renormalized in the RI and the $\overline{\text{MS}}$ schemes, we use the matching factor, $C_O^{\text{RI}}(\mu_0) = Z_O^{\overline{\text{MS}}}(\mu_0)/Z_O^{\text{RI}}(\mu_0)$ at a matching scale μ_0, which

TABLE I.   Summary of types of the RI schemes.

Type	Kinematics	Projection operator
RI/MOM	$p_1 = p_2, q = 0$	Equal to Γ^O
RI/SMOM	$p_1^2 = p_2^2 = q^2$	Equation (24)
RI/SMOM$_{\gamma_\mu}$	$p_1^2 = p_2^2 = q^2$	Equal to Γ^O

is computed under the Landau gauge in the perturbation theory with help of the renormalization group as detailed in Appendix C. The two-loop results for the matching factor have been already obtained for the RI/SMOM$_{(\gamma_\mu)}$ scheme in Ref. [33], while the three-loop result was known for the RI/MOM scheme [34,35]. In addition, the evolution factor $R_O(\mu, \mu_0) = Z_O^{\overline{\text{MS}}}(\mu)/Z_O^{\overline{\text{MS}}}(\mu_0)$ from the matching scale μ_0 to a reference scale μ in the $\overline{\text{MS}}$ scheme, is calculated with the four-loop beta function and the three-loop anomalous dimension. Combining the matching factor and the evolution factor, the conversion from $Z_O^{\text{RI}}(\mu_0)$ to $Z_O^{\overline{\text{MS}}}(\mu)$ can be achieved at next-to-next-to-leading (NNLO) accuracy for both the RI/MOM and RI/SMOM$_{(\gamma_\mu)}$ schemes as

$$Z_O^{\overline{\text{MS}}}(\mu) = R_O(\mu, \mu_0) \cdot C_O^x(\mu_0)$$
$$\times Z_O^x(\mu_0) : x \in \left\{ \begin{array}{c} \text{RI/MOM} \\ \text{RI/SMOM}_{(\gamma_\mu)} \end{array} \right\}. \quad (25)$$

In this study, we determine the renormalization constants by mainly using the RI/SMOM$_{(\gamma_\mu)}$ scheme that can suppress the unwanted infrared effects as will be described in Sec. III B 2, while detailed comparisons between the RI/MOM and RI/SMOM$_{(\gamma_\mu)}$ schemes are provided in Appendix A.

B. Residual scale dependence

In general, however, the value of $Z_O^{\overline{\text{MS}}}(\mu)$ obtained from $Z_O^{\text{RI}}(\mu_0)$ in Eq. (25) receives the residual dependence on the choice of the matching scale μ_0. As explained previously, in the RI scheme, the renormalization scale μ_0 is introduced by the external momentum p as $\mu_0 = \sqrt{p^2}$. For the higher matching scale μ_0, the perturbation theory becomes relevant and the correct scaling behavior of the renormalization constants is well predicted by the perturbation theory with help of the renormalization group. However, there is one issue at higher momenta p due to the presence of the lattice artifacts, which are associated with the discretization errors of $\mathcal{O}((ap)^{2n})$ in the lattice quark propagator $S(p|x)$. On the other hand, the error associated with the truncation of the perturbative series at a given order grows as the momenta p decrease. Furthermore, if some nonperturbative effect is introduced at lower momenta p, the effect cannot be corrected by perturbation theory and fails the matching. This is the window problem, which arises as the

renormalization scale $\mu_0 = \sqrt{p^2}$ in the RI scheme. An ideal situation is realized if the window is sufficiently wide ($\Lambda_{\text{QCD}} \ll \mu_0 \ll \mathcal{O}(a^{-1})$). However in practice one needs to deal with the both edges of the window, and then associated systematic uncertainties need to be carefully studied.

In summary, there are three sources for the residual scale dependence as below.

(1) Lattice discretization artifacts at higher μ_0.
(2) Unwanted infrared effects at lower μ_0.
(3) Truncation errors in perturbation matching and evolution at lower μ_0.

The first and second points cause the peculiar behavior as a function of μ_0. The former functional form can be represented by a positive power series in $(a\mu_0)^2$, while the latter point can be incorporated in the functional form that contains the negative power term of μ_0. Here, our aim is to extract the relevant μ_0-independent value as the final result of $Z_O^{\overline{\text{MS}}}(\mu)$. The truncation error, however, is not avoided if the perturbation theory is used. Therefore, we will also evaluate the systematic uncertainties associated with the third point after extracting μ_0-independent value. In the following subsections, we describe how to reduce the systematic uncertainties associated with the residual μ_0-dependence, which are mainly caused by the first and second points, so as to extract the relevant μ_0-independent value.

1. Lattice artifacts

The renormalization constants should have the lattice artifacts stemming from the lattice discretization. They are associated with the $H(4)$ hypercubic symmetry in the lattice discretization, which breaks $O(4)$ invariance. There are four types of invariants: $p^{[2n]} = \sum_\mu p_\mu^{2n}$ for $n = 1, 2, 3, 4$, under the $H(4)$ symmetry [36]. The higher-order invariants $p^{[4]}$, $p^{[6]}$, and $p^{[8]}$ correspond to the non $O(4)$ invariants, whose presence calls the hypercubic artifacts [36]. Therefore, the lattice quark propagator is no longer expressed by the single variable function of $p^2 = p^{[2]}$, and then will form a "fish-bone structure." It is empirically known that Wilson fermions show less-pronounced structure than chiral fermions, and thus develop less problematically [36]. In this study, we simply adopted the following "democratic" strategy. First, we impose a "cylindrical" cut on the values of momenta and then minimize the $O(4)$ variant hypercubic artifacts. We take an average over the selected momentum configurations, so that the single-valued function of p^2 can be obtained.

As described earlier, the renormalization scale μ_0 is introduced according to the subtraction kinematics with the external quark momenta p as $\mu_0 = \sqrt{p^2}$ in determination of the renormalization constant from the vertex function. The lattice artifacts can be described by the polynomial function of the dimensionless variable $(a\mu_0)$ as

$$Z_O(\mu_0) \approx \sum_{k>0}^{k_{\max}} c_k(a\mu_0)^{2k}, \qquad (26)$$

where the odd power terms do not present under the momentum reflection symmetry ($p \to -p$) for the external momentum. We will adopt the above functional form to subtract the lattice discretization artifacts caused by the finite lattice spacing a at higher μ_0 and then estimate the relevant μ_0-independent value c_0. The selection of the range of μ_0 and the choice of the number of the polynomial terms ($k_{\max}$) may introduce systematic uncertainties. Therefore, we will make a detailed assessment of such the systematic uncertainties in order to determine the systematical errors on the final result of the μ_0-independent value.

2. Unwanted infrared divergence

There is another major source of systematic uncertainties associated with the *infrared* physics scale Λ_{IR}. In the quark sector, typical IR scales come from quark mass m_q ($\sim\Lambda_{\mathrm{IR}}$), chiral condensate $\langle \bar{q}q \rangle$ ($\sim\Lambda_{\mathrm{IR}}^3$) and so on. The infrared divergence can remain even in the chiral limit due to nonperturbative vacuum condensates. It is demonstrated in the RI/MOM scheme [31], that $\langle \bar{q}q\bar{q}q \rangle$ condensate contributes at $O(\mu_0^{-2})$ by using the Weinberg's power counting (necessary dimensional adjustment is done using Λ_{QCD} as a typical low energy momentum scale triggering the condensate) [37]. This particular contribution is, however, removed by the use of SMOM schemes. Although large infrared effect is much reduced in SMOM schemes in this way, there is no guarantee that all the $O(\mu_0^{-2})$ effects are completely removed. Indeed it is pointed out [38] that the vertex functions also may receive from the dimension two condensate contribution ($\Lambda_{\mathrm{IR}}^2 = \langle A^2 \rangle$) since $\langle A^2 \rangle$ condensate could couple to the quark propagator in the case of the Landau gauge, which is suggested in the RI' scheme [38] whose wave function renormalization is equivalent to the RI/SMOM scheme [32]. As the leading infrared effect we take a double pole with respect to μ_0

$$Z_O(\mu_0) \approx \frac{c_{-1}}{(\Lambda_{\mathrm{IR}}^{-1}\mu_0)^2}, \qquad (27)$$

where a scale Λ_{IR} is responsible for characterizing infrared physics.

3. Uncertainties from perturbation and others

As described earlier, in order to compare with the experimental values, we have to evaluate the renormalized values in the $\overline{\mathrm{MS}}$ at the renormalization scale of 2 GeV using the continuum perturbation theory for the scheme matching and the scaling evolution. Therefore, we would like to estimate possible truncation errors in perturbation matching and evolution. To this end, we utilize the two intermediate schemes where the conversion factors differ.

A difference of resulting renormalization factors through RI/SMOM and RI/SMOM$_{\gamma_\mu}$ schemes may be interpreted as a truncation error. We have four results of renormalization factor for each operator. They are given through the four combinations with the choices of two types of the SMOM scheme, which purely care the truncation error, combined with two ways of estimating the wave function renormalization through the vector vertex Λ_V or axial-vector vertex Λ_A with help of Z_V^{SF} or Z_A^{SF}.

It is worth remarking that there is no difference between Λ_V and Λ_A in the continuum perturbation theory. Therefore, the difference that occurs only when choosing the vector or axial-vector with a fixed choice of the SMOM scheme does not originate from the truncation error and rather arises from other sources of nonperturbative effects. Indeed, such difference in the RI/MOM scheme becomes sizable due to unwanted infrared divergence associated with nonperturbative effects as discussed in Appendix A. The above-mentioned difference is already suppressed by means of the SMOM schemes, and then is expected to be subdominant. In this study, we simply assume that a typical size of systematic uncertainties associated with the truncation error can be explored by the difference among the four combinations with the choices of the intermediate schemes (RI/SMOM or RI/SMOM$_{\gamma_\mu}$ schemes), combined with two inputs of Z_V^{SF} or Z_A^{SF}. We confirm that the estimated uncertainties are comparable with the naive truncation error $\mathcal{O}(\alpha_s^3) \sim 3\%$ and this alternative estimation works, as detailed in Appendix B.

C. Renormalization constants

In order to reduce the systematic uncertainties associated with the residual μ_0-dependence, let us introduce two types of fitting functional forms as a function of the matching scale μ_0. The first functional form which includes both the infrared divergent contribution at lower μ_0 and the discretization corrections at higher μ_0 is given as

$$f_{\mathrm{Global}}(\mu_0) = \frac{c_{-1}}{(\Lambda_{\mathrm{IR}}^{-1}\mu_0)^2} + c_0 + \sum_{k>0}^{k_{\max}} c_k(a\mu_0)^{2k} \quad (28)$$

with c_0 being the μ_0-independent value of $Z_O^{\overline{\mathrm{MS}}}(\mu)$ at the renormalization scale $\mu = 2$ GeV. Equation (28) is used for the global fit to a wide range of μ_0 (denoted as "Global" in subscript). In this fit model, the leading contribution at lower μ_0 is simply introduced by a double pole with respect to a dimensionless variable of $\Lambda_{\mathrm{IR}}^{-1}\mu_0$, where a scale Λ_{IR} is responsible for characterizing infrared physics. A model dependence that is mainly introduced by the double pole term should be addressed.

In this context, we use different fitting strategy to assess the systematic error associated with the model dependence of the fit form (28). For the sake of this purpose, we use the second functional form

$$f_{\text{IR-trunc.}}(\mu_0) = c_0 + \sum_{k>0}^{k_{\max}} c_k (a\mu_0)^{2k}, \qquad (29)$$

where only positive power series in $(a\mu_0)^2$ are included. This functional form is widely used in the previous studies [13–17]. We then apply the functional form of Eq. (29) for fitting the data in a restricted range $\mu_0 \gg \Lambda_{\text{IR}}$ (denoted as "IR-trunc." in subscript) for avoiding unwanted infrared effects. However, the fit result would be sensitive to the fit range ($\mu_{\min} \leq \mu_0 \leq \mu_{\max}$), especially the choice of $\mu_{\min}$ that is supposed to satisfy $\mu_{\min} \gg \Lambda_{\text{IR}}$. In this study, the fitting with Eq. (29) is only applied to the case of $\mu_{\min} \geq 2$ GeV, where the truncation errors in perturbation matching can be simultaneously reduced.

Using two functional forms of Eqs. (28) and (29), the appropriate fit range ($\mu_{\min} \leq \mu_0 \leq \mu_{\max}$) with a smaller value of $k_{\max}$ is carefully determined by means of uncorrelated fits according to the following guidelines:

   (I) c_0 is insensitive to the variation of the fit range.
   (II) $k_{\max}$ ensures that inclusion of the higher power terms does not change the value of c_0.
   (III) χ^2/dof is close to unity as much as possible.

If the above two fit procedures lead to compatible results, both the model dependence in the determination of the μ_0-independent value with the usage of Eq. (28) and the strong dependence of the fit range using Eq. (29) are reasonably well under control. A representative value is selected from them as the central value of the final result, while discrepancies among them can be estimated as systematic errors.

In this study, three types of systematic uncertainties for the determination of the renormalization constant are examined as follows:

   (1) $(\Delta Z)_{\text{fit}}$ is determined by the maximum difference among the fit results that are stable against the variation of the fit range and the choice of $k_{\max}$.
   (2) $(\Delta Z)_{\text{scheme}}$ is determined from the maximum difference among the four combinations with the choices of the intermediate schemes (RI/SMOM or RI/SMOM$_{\gamma_\mu}$ schemes) combined with the SF inputs of Z_V and Z_A (hereafter denoted as $\{$SF input, scheme$\} = \{Z_V, \text{SMOM}\}$, $\{Z_V, \text{SMOM}_{\gamma_\mu}\}$, $\{Z_A, \text{SMOM}\}$, $\{Z_A, \text{SMOM}_{\gamma_\mu}\}$).
   (3) $(\Delta Z)_{\text{model}}$ is determined by discrepancy between results obtained from the global fit with the functional form of $f_{\text{Global}}(\mu_0)$ and the IR-truncated fit with the functional form of $f_{\text{IR-trunc.}}(\mu_0)$ with the optimal combination of $\{$SF input, scheme$\}$.

Furthermore, all three systematic uncertainties are added in quadrature to get

$$(\Delta Z)_{\text{syst}} = \sqrt{((\Delta Z)_{\text{fit}})^2 + ((\Delta Z)_{\text{scheme}})^2 + ((\Delta Z)_{\text{model}})^2}. \qquad (30)$$

We then will quote the total error of the renormalization constant as

$$(\Delta Z)_{\text{total}} = \sqrt{((\Delta Z)_{\text{stat}})^2 + ((\Delta Z)_{\text{syst}})^2}, \qquad (31)$$

which is given by both statistical and systematic uncertainties combined in quadrature.

IV. SIMULATION DETAILS

In this paper, we use two ensembles of gauge configurations, which are generated by the PACS Collaboration with $L^3 \times T = 128^3 \times 128$ and $64^3 \times 64$ lattices using the six stout-smeared $O(a)$-improved Wilson quark action and the Iwasaki gauge action [39] at fixed gauge coupling $\beta = 1.82$ corresponding to the lattice spacing of $a = 0.08520(16)$ fm $[a^{-1} = 2.3162(44)$ GeV] determined from the Ξ baryon mass input [40]. The stout-smearing parameter is set to $\rho = 0.1$ [41]. The improved coefficient, $c_{\text{SW}} = 1.11$, is nonperturbatively determined using the Schrödinger functional (SF) scheme [42]. The PACS Collaboration has performed the finite-size study for light meson and baryon sectors at the physical point in $2 + 1$ flavor QCD with the two lattices [40,43]. A brief summary of the simulation parameters for the two lattice volumes is given in Table II.

As pointed out in Ref. [40], the two volumes (linear spatial extents of 10.9 fm and 5.5 fm) are large enough for the finite-size effect on the nucleon mass to be negligible. Even for the nucleon matrix elements, the finite-size effects are hardly detected under the current statistical precision [21]. Thanks to the large spatial volume ($L = 128$), the small momentum transfer region close to the zero momentum transfer, $q^2 = 0$ can be accessible in calculation of the various hadron form factors. Therefore, the $L = 128$ lattice was utilized for studies of the nucleon form factors [23] and also the K_{l3} form factor [44], both of which require the q^2 interpolation (or extrapolation) to the zero momentum point. In this work, we use 20 gauge configurations separated by 10 molecular dynamics trajectories for the $L = 128$ lattice, while 100 gauge configurations separated by 20 molecular dynamics trajectories are used for the $L = 64$ lattice. Their statistical errors are estimated by the single elimination jackknife method. Significant reduction of the computational cost is achieved by employing the all-mode-averaging (AMA) method [45–47] with the deflated Schwartz alternating process (SAP) [48] and generalized

TABLE II. Parameters of $2 + 1$ flavor PACS ensembles with two different lattice volumes. See Refs. [40,43] for further details.

β	$L^3 \times T$	a^{-1} (GeV)	κ_{ud}	κ_s	M_π (GeV)
1.82	$128^3 \times 128$	2.3162(44)	0.126117	0.124902	0.135
1.82	$64^3 \times 64$	2.3162(44)	0.126117	0.124902	0.138

TABLE III.　Details of the measurements: the spatial extent (L), time separation (t_{sep}), type of the smearing method, smearing parameters of the quark operator, the stopping condition of quark propagator in the high- and low-precision calculations (ϵ_{high} and ϵ_{low}), the number of measurements for the high- and low-precision calculations (N_{org} and N_G), the number of configurations (N_{conf}) and the total number of the measurements ($N_{\text{meas}} = N_G \times N_{\text{conf}}$), respectively.

L	t_{sep}	Smearing-type	Smearing parameters	ϵ_{high}	ϵ_{low}	N_{org}	N_G	N_{conf}	N_{meas}
128	10	Exp.(I)	$(A, B) = (1.2, 0.16)$	10^{-8}	—[a]	1	128	20	2,560
	12			10^{-8}	—[a]	1	256	20	5,120
	14			10^{-8}	—[a]	2	320	20	6,400
	16			10^{-8}	—[a]	4	512	20	10,240
	13	Gauss	$(n_G, w_G) = (110, 8.0)$	10^{-8}	—[a]	1	128	20	2,560
	16			10^{-8}	—[a]	6	450	20	9,000
64	11	Exp.(I)	$(A, B) = (1.2, 0.16)$	10^{-8}	0.005	4	40	50	2,000
	14			10^{-8}	0.02	4	64	100	6,400
	12	Exp.(II)	$(A, B) = (1.2, 0.14)$	10^{-8}	0.005	4	256	100	25,600
	14			10^{-8}	0.005	4	1,024	100	102,400
	16			10^{-8}	0.002	4	2,048	100	204,800

[a]As for the $L = 128$ lattice, the low-precision calculations use a fixed number of iterations for the stopping condition as 5 GCR iterations using 8^4 SAP domain size with 50 deflation fields.

conjugate residual (GCR) [49] for the measurements as in our previous works [21,22]. We compute the combination of the correlation function with high-precision $O^{(\text{org})}$ and low-precision $O^{(\text{approx})}$ as

$$O^{(\text{AMA})} = \frac{1}{N_{\text{org}}} \sum_{f \in G}^{N_{\text{org}}} (O^{(\text{org})f} - O^{(\text{approx})f}) + \frac{1}{N_G} \sum_{g \in G}^{N_G} O^{(\text{approx})g},$$

(32)

where the superscripts f, g denote the transformation under the lattice symmetry G. In our calculations, it is translational symmetry, e.g., changing the position of the source operator, and changing the temporal direction of the configuration using its hypercubic symmetry as in Refs. [23,40,43,44]. N_{org} and N_G are the numbers for $O^{(\text{org})}$ and $O^{(\text{approx})}$, respectively. The numbers and the stopping conditions of the quark propagator for the high- and low-precision measurements are summarized in Table III.

In calculation of the nucleon 2- and 3-point functions, we use the same quark action as in the gauge configuration generation with the hopping parameter $\kappa = 0.126117$ for the degenerated up-down quarks, the improved coefficient, $c_{\text{SW}} = 1.11$, and six steps of stout-smearing to the link variables. The periodic boundary condition in all the temporal and spatial directions is adopted in the quark propagator calculation.

The quark propagator is calculated using the exponential smeared source (sink) with the Coulomb gauge fixing. The smearing parameters for the quark propagator defined in Eq. (5) are chosen as $(A, B) = (1.2, 0.16)$ for the $L = 128$ lattice [22] and $(A, B) = (1.2, 0.14), (1.2, 0.16)$ for the $L = 64$ lattice [21]. In addition to the exponential source

(sink), we also use the gauge-covariant, approximately Gaussian-shaped source (sink) [24] for the $L = 128$ lattice with a single parameter set of $(n_G, w_G) = (110, 8.0)$, which is defined in Eq. (6), so as to make sure that there is no dependence on the gauge fixing condition and the excited-state contamination is well controlled on our final results. All parameters of adopted sources are chosen to optimize the effective mass plateau for the smear-local case in each of $L = 128$ and $L = 64$ lattices.

The nucleon 3-point functions are calculated using the sequential source method with a fixed source-sink separation [27,50]. This method requires the sequential quark propagator for each choice of a projection operator $\mathcal{P}_k$ regardless of the types of current J^O. To minimize the numerical cost for the larger volume calculation ($L = 128$), we have to restrict ourselves to calculating a single 3-point function with the projection $\mathcal{P}_{5z}$, while we calculate three 3-point functions with the projection $\mathcal{P}_{5j}$ in all the three spatial directions $j = x$, y, z for the smaller volume calculation ($L = 64$). Furthermore, in the case of the $L = 64$ volume, we also take the average of the forward and backward 3-point functions to increase statistics.

As for the source-sink separation of t_{sep} (denoted as $t_{\text{sep}} = t_{\text{sink}} - t_{\text{src}}$), we use four variations of $t_{\text{sep}} = 10, 12, 14, 16$ with the exponential source[4] and two variations of $t_{\text{sep}} = 13, 16$ with the gauge-covariant Gaussian source for the $L = 128$ lattice, while four variations of $t_{\text{sep}} = 11, 12, 14, 16$ for the $L = 64$ lattice as also summarized in Table III. We investigate the effects of

---

[4]For $t_{\text{sep}} = 16$, we include additional numerical simulations which lead to a slightly larger number of measurements in comparison to our earlier work [22].

the excited-state contamination by varying t_{sep} from 0.85 to 1.36 fm in the standard plateau method that was explained in Sec. II B.

The renormalization constants for vector and axial-vector currents, $Z_O(O = V, A)$ are obtained with the SF scheme at vanishing quark mass as $Z_V = 0.95153(76)(1487)$ and $Z_A = 0.9650(68)(95)$, where each error represents statistical and systematic error stemming from the difference between two volumes [29]. However, the second errors are simply ignored in the later analysis, since we choose the larger volume [29] to set the physical scale. As for the renormalization of other quark bilinears, scalar and tensor currents, we employed the RI scheme for their intermediate scheme, using quark propagators which are nonperturbatively calculated on the $L = 64$ lattice with the Landau gauge fixing. The details of them are described in Sec. III.

V. NUMERICAL RESULTS

In this section we present the isovector couplings of the nucleon for the vector, axial, scalar and tensor channels, obtained from both 128^4 and 64^4 lattices. We will first show results of the bare couplings, which can be determined by the plateau measured in the ratio defined in Eq. (13). For the renormalization of the scalar and tensor channels, we use the $\text{RI/SMOM}_{(\gamma_\mu)}$ schemes as the intermediate scheme and then evaluate the renormalized values of the scalar and tensor couplings in the $\overline{\text{MS}}$ scheme at the renormalization scale of 2 GeV with the help of perturbation theory of the matching between the intermediate and $\overline{\text{MS}}$ schemes.

A. Bare coupling

The bare coupling can be read off from the ratio (13) as the asymptotic plateau that is independent of a choice of t_{op},
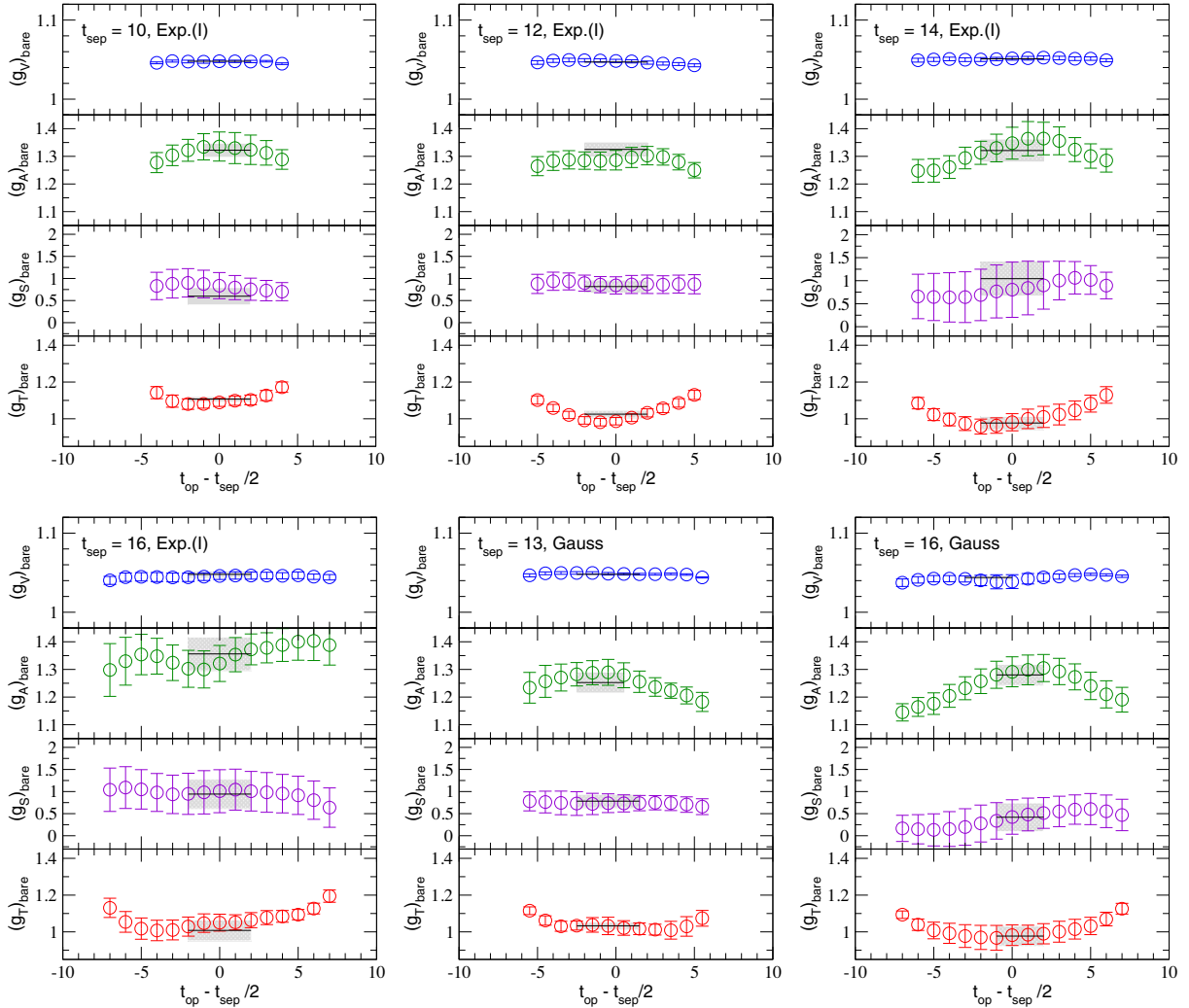

FIG. 1. Bare coupling g_O for $O = V, A, S, T$ obtained from the 128^4 lattice as a function of the current operator insertion point t_{op}. In each panel, the results for the bare values of g_V, g_A, g_S, and g_T are plotted from top to bottom with different choices of t_{sep} and smearing type. For the sake of comparison, the interval of the y axis in each channel is selected to be the same for all the panels. The solid line represents the average value, and shaded band displays the fit range and one standard deviation. The value of t_{sep} and type of smearing are given in the legends.
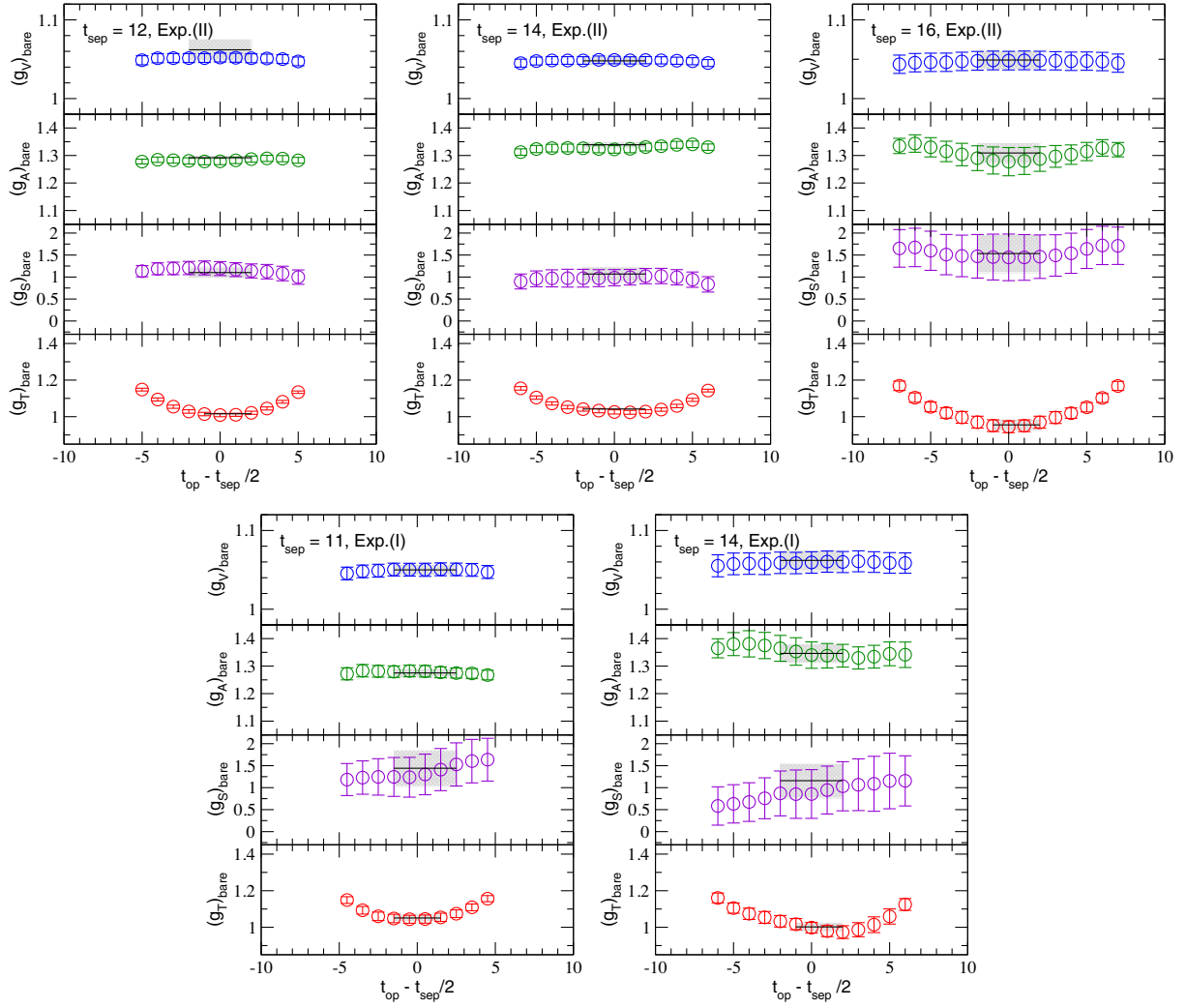
FIG. 2. Bare coupling g_O for $O = V, A, S, T$ obtained from the 64^4 lattice as a function of the current operator insertion point t_{op}. The rest is the same as in Fig. 1.

with some moderate source-sink separation t_{sep} and the optimal choice of the smearing parameters. Since the excited-state contaminations could not be fully eliminated by tuning smearing parameters in practice, one should calculate the ratio (13) with several choices of t_{sep}, and then makes sure whether the evaluated value of the bare coupling does not change with a variation of t_{sep} within a certain precision.

In Fig. 1, we show results of the bare couplings obtained from the $L = 128$ lattice for different choices of t_{sep} and two kinds of the smearing-type. In each panel, the results for the bare values of g_V, g_A, g_S and g_T are plotted from top to bottom as a function of the current operator insertion point t_{op}. At a glance, plateau behaviors are observed for all four channels in the middle region between the source and sink points, thanks to our elaborate tuning of the smearing parameters.

We also show the bare couplings obtained from the $L = 64$ lattice in Fig. 2. The exponential smearing is only

used with two sets of smearing parameters, $(A, B) = (1.2, 0.14)$ and $(1.2, 0.16)$. The former set is obtained by retuning for the $L = 64$ lattice [denoted as Exp.(II)], while the latter set is the same as the one used in the previous $L = 128$ calculation [denoted as Exp.(I)].

Let us focus on the upper three panels in Fig. 2, where the symmetric behavior with respect to t_{op} is clearly seen in all four channels. It is worth reminding that in the $L = 64$ calculation, the time-reversal average was implemented in our averaging procedure on each configuration with multiple measurements, which includes both forward and backward propagations in time, as described early. More importantly, it is clearly observed that there is some channel dependence. The vector, axial-vector and scalar channels show the very long plateau behavior up to the vicinity of the source and sink points, while the tensor channel exposes the residual t_{op} dependence that would be originated from the excited-state contaminations. This tendency is slightly seen in the $L = 128$ calculations, where the symmetric

TABLE IV. Results of the bare couplings g_O for $O = V, A, S, T$ obtained from both 128^4 and 64^4 lattices with different choices of the source-sink separation (t_{sep}) and the smearing type. The values of the bare couplings are extracted by the correlated constant fit on the relevant ratio (13) with the fit range, which is denoted as the gray-shaded area in each panel of Figs. 1 and 2.

L	t_{sep}	Smearing-type	g_V^{bare}	g_A^{bare}	g_S^{bare}	g_T^{bare}
128	10	Exp.(I)	1.048(1)	1.322(25)	0.599(197)	1.107(14)
	12		1.047(2)	1.325(23)	0.817(147)	1.025(21)
	14		1.051(2)	1.321(38)	1.044(353)	0.977(36)
	16		1.048(4)	1.356(61)	0.943(336)	1.008(57)
	13	Gauss	1.048(1)	1.252(34)	0.783(153)	1.033(20)
	16		1.044(2)	1.280(38)	0.418(325)	0.977(54)
64	11	Exp.(I)	1.050(7)	1.275(16)	1.442(417)	1.051(21)
	14		1.062(13)	1.346(35)	1.159(395)	1.002(26)
	12	Exp.(II)	1.062(14)	1.292(9)	1.102(127)	1.016(8)
	14		1.048(4)	1.339(12)	1.068(168)	1.042(9)
	16		1.049(12)	1.309(38)	1.535(436)	0.955(32)

behavior would be hindered by larger statistical fluctuations because each total number of the measurements with the $L = 128$ lattice is much smaller than the cases of Exp.(II) with $t_{\text{sep}} = 12, 14, 16$ in the $L = 64$ calculations.

Although the asymptotic plateau behavior is relatively shortened in the tensor channel, there is still room for extracting the value of the bare coupling from the plateau behavior appearing in the middle region between the source and sink points even in the $L = 64$ calculations. We simply use the correlated constant fit to extract the value of the bare coupling for all channels in both $L = 128$ and $L = 64$ calculations. In the $L = 128$ calculations, we choose the same fit range that is determined by the axial-vector channel, while the narrower fit range is adopted for the tensor channel in the $L = 64$ calculations where the small statistical fluctuations make it difficult to perform the constant fit with the same fit range used for the other channels. The fit ranges, which are carefully chosen to obtain a reasonable value of χ^2/dof, are denoted as gray-shaded areas in each panel of both figures. The obtained values of the bare couplings are summarized in Table IV.

B. Renormalization

In order to compare with the experimental values or other lattice results, the bare couplings g_S and g_T should be renormalized with the renormalization constants in the $\overline{\text{MS}}$ scheme, while the renormalization constants for vector and axial-vector current, $Z_O(O = V, A)$ are obtained with the SF scheme at vanishing quark masses as $Z_V^{\text{SF}} = 0.95153(76)$ and $Z_A^{\text{SF}} = 0.9650(68)$ [29]. For the scalar and tensor cases, we use the RI scheme as the intermediate scheme in order to evaluate the renormalization constants $Z_O^{\text{RI}}(O = S, T)$ in fully nonperturbative manner with the value of $Z_O^{\text{SF}}(O = V, A)$ as shown in Eq. (23). The resulting renormalization constants are then converted to the $\overline{\text{MS}}$ scheme at an intermediate scale and evolved to the scale of

2 GeV using the perturbation theory as described in Eq. (25).

The smaller volume ensemble ($L = 64$) with 101 gauge configurations is used for computing the renormalization constants. Averaging the results of the vertex functions over multiple sources would help to reduce the statistical uncertainties. The vertex functions can be constructed by the (Fourier-transformed) quark propagator on each gauge configuration. The quark propagator is calculated by using a point source since all modes in the momentum space are equally taken into account. We then calculate the quark propagator with four different source locations at $x_0 = (0, 0, 0, 0)$, (16, 16, 16, 16), (32, 32, 32, 32), (48, 48, 48, 48). In the analysis, all four sets of vertex functions are folded together to create the single-vertex functions, respectively.

1. Test for the chiral symmetry

Our calculations are performed with the stout-smeared $O(a)$ improved Wilson fermions, where the chiral symmetry is explicitly broken even at vanishing quark masses due to the discretization error. This is indeed confirmed by the fact of $Z_V^{\text{SF}} \neq Z_A^{\text{SF}}$ for the local currents. In order to examine the explicit chiral symmetry breaking in the RI scheme, we introduce the following quantity

$$c_{V-A} \equiv \frac{\tilde{\Lambda}_A^x - \tilde{\Lambda}_V^x}{(\tilde{\Lambda}_A^x + \tilde{\Lambda}_V^x)/2}, \tag{33}$$

where $\tilde{\Lambda}_{V(A)}^x$ denotes the traced vertex function with an appropriate projection operator as $\tilde{\Lambda}_{V(A)}^x = \text{Tr}[\Lambda_{V(A)} \mathcal{P}_{V(A)}^x]$ for $x = \text{SMOM}$ or SMOM_{γ_μ}. Nonzero value of c_{V-A} directly indicates a violation of the equality $Z_V = Z_A$, since the value of c_{V-A} turns out to be the ratio of $\frac{Z_V - Z_A}{(Z_V + Z_A)/2}$. However recall that the vertex functions receive
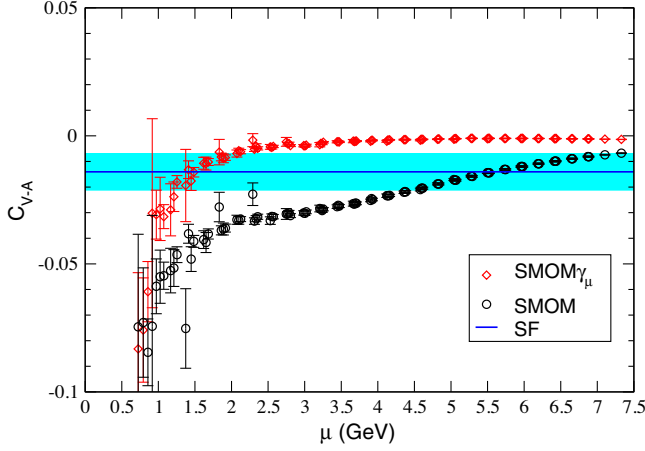
FIG. 3. A plot of c_{V-A} as a function of μ showing that the effects of the explicit chiral symmetry breaking tend to be small in high μ region. The blue line and shaded band represent the reference value and its uncertainty given by the SF scheme.

the effects from both the explicit chiral symmetry breaking and spontaneous chiral symmetry breaking [51].

The results obtained from the SMOM (black circles) and SMOM$_{\gamma_\mu}$ (red diamonds) schemes are shown in Fig. 3. The blue line and shaded band represent the reference value and its uncertainty given by the SF scheme as

$$c_{V-A}^{\text{SF}} = \frac{Z_V^{\text{SF}} - Z_A^{\text{SF}}}{(Z_V^{\text{SF}} + Z_A^{\text{SF}})/2} = -0.0141(71), \qquad (34)$$

which is scale independent. The sizes of c_{V-A} for both results of SMOM and SMOM$_{\gamma_\mu}$ except for the lower μ region ($\mu < 1.5$ GeV) are equally small compared to the SF value c_{V-A}^{SF} as being less than about 5%. The result of SMOM shows slightly stronger dependence of the renormalization scale than that of SMOM$_{\gamma_\mu}$, while the data of SMOM gradually approaches an asymptotic value of SMOM$_{\gamma_\mu}$ at high scale as the scale μ increases. The asymptotic value of c_{V-A} obtained in the RI scheme is expected to be the same as the SF value, which should be independent of the renormalization scheme, when c_{V-A} is evaluated at vanishing quark masses. Recall that c_{V-A} evaluated in the RI scheme is calculated at the physical point, where the light quark mass is small but finite. This deviation from the SF value is supposed to be contributions from explicit chiral symmetry breaking due to the finite quark mass. On the other hand, the strong scale dependence observed in low μ region for both SMOM and SMOM$_{\gamma_\mu}$ should be considered as the infrared divergent effect due to both the explicit chiral symmetry breaking and spontaneous chiral symmetry breaking [51]. These observations therefore indicate that our action indeed achieves $\mathcal{O}(a)$ improvement and then discretization uncertainties are expected to be suppressed being less than a few % according to the

value of c_{V-A}^{SF}. Thus, the framework of the Rome-Southampton method to evaluate the renormalization constants is applicable even for Wilson-type fermions being highly improved in this study.

2. Residual matching scale dependence and systematic uncertainties

We show the renormalization constants for the scalar and tensor current operators evaluated in the $\overline{\text{MS}}$ scheme at the scale of 2 GeV in Figs. 4 and 5. Similar results are obtained for the four combinations of {SF input, scheme}. As discussed in Sec. III B, these figures clearly show the residual dependence of the choice of the matching scale μ_0 in the final results of $Z_O^{\overline{\text{MS}}}(\mu)$ at the renormalization scale $\mu = 2$ GeV ($O = S$ or T), which are given by Eq. (25) with the input values of $Z_O^{\text{RI}}(\mu_0)$. We therefore evaluate the μ_0-independent value of $Z_O^{\overline{\text{MS}}}(2 \text{ GeV})$ by the analysis described in Sec. III C.

In each panel of Figs. 4 and 5, red and blue curves with error bands represent two fit results obtained from the global fit (28) and the IR-truncated fit (29) with $k_{\max} = 2$, while green curve with error bands is given by removing the divergent contribution from the global fit result. The intersections of the green and blue curves with the y-axis correspond to the μ_0-independent contributions obtained from both the global and IR-truncated fit results. For the sake of clarity, we plot their central values and statistical errors denoted as the circle and squared symbols, which are slightly shifted from the y-axis in each panel of Figs. 4 and 5. Both results obtained from two different fit procedures, where the unwanted infrared divergence is treated in a different way, coincide each other with the optimal choices of the fit range of $[\mu_{\min} : \mu_{\max}]$ for each fit as will be discussed as follows.

First, we check the stability of c_0, which is the μ_0-independent term obtained from either the global fit with Eq. (28) or the IR-truncated fit with Eq. (29), with variation of $\mu_{\min}$ under the condition of $k_{\max} = 2$ with three values of $\mu_{\max} = 3, 4$, and 5 GeV as shown in Figs. 6 and 7. Figure 6 shows the results for $Z_S^{\overline{\text{MS}}}(2 \text{ GeV})$ in the cases of the four combinations of {SF input, scheme} as a function of $\mu_{\min}$, while Fig. 7 presents the results for $Z_T^{\overline{\text{MS}}}(2 \text{ GeV})$. The diamond and circle symbols are obtained from the global fit and the IR-truncated fit, respectively.

The former fit results are restricted in the range of $\mu_{\min} \leq 2$ GeV (left side of vertical dashed line), while the latter fit results are given with the condition of $\mu_{\min} > 2$ GeV (right side of vertical dashed line). The red, black, and blue symbols represent the results given with the fixed value of $\mu_{\max} = 3, 4$, and 5 GeV, respectively. At a glance, the c_0 value is sensitive to the choice of $\mu_{\min}$ in the case of $\mu_{\max} = 3$ GeV with $k_{\max} = 2$. However, the larger values of $\mu_{\max}$ tend to ensure the stability of the c_0 value since the
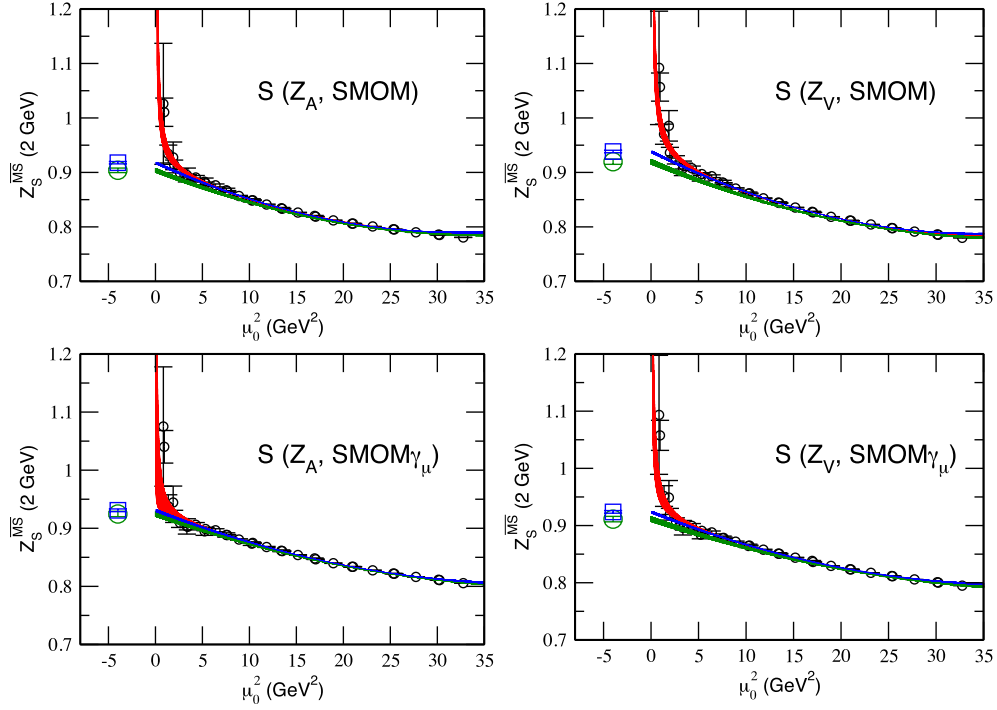
FIG. 4. The renormalization constant for the scalar current operator evaluated in the $\overline{\text{MS}}$ scheme at a scale of 2 GeV as a function of the square of the matching scale μ_0. Similar results are obtained for the four combinations of {SF input, scheme} = {Z_V, SMOM} (right upper panel), {Z_V, SMOM$_{\gamma_\mu}$} (right lower panel), {Z_A, SMOM} (left upper panel), {Z_A, SMOM$_{\gamma_\mu}$} (left lower panel). In each panel, red and blue curves with error bands represent two fit results obtained from the global fit and the IR-truncated fit with $k_{\text{max}} = 2$, while green curve is given by removing the divergent contribution from the global fit result (red curve). The blue circle and green squared symbols are the μ_0-independent contributions obtained from both the global and IR-truncated fit results.
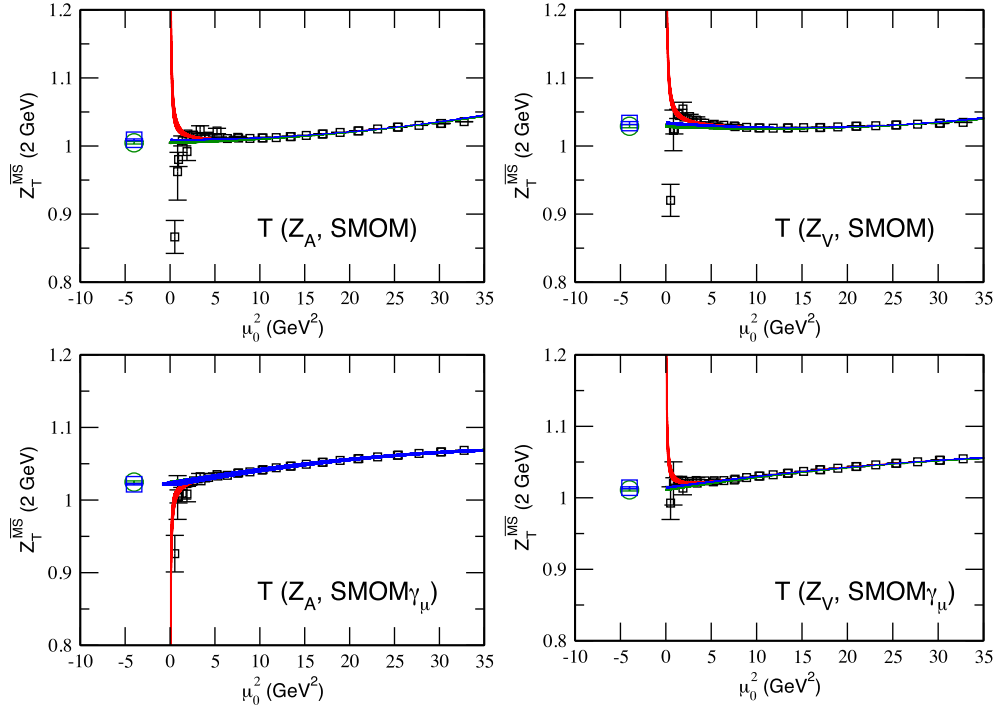

FIG. 5. The renormalization constant for the tensor current operator evaluated in the $\overline{\text{MS}}$ scheme at a scale of 2 GeV as a function of the square of the matching scale μ_0. The rest is the same as in Fig. 4.
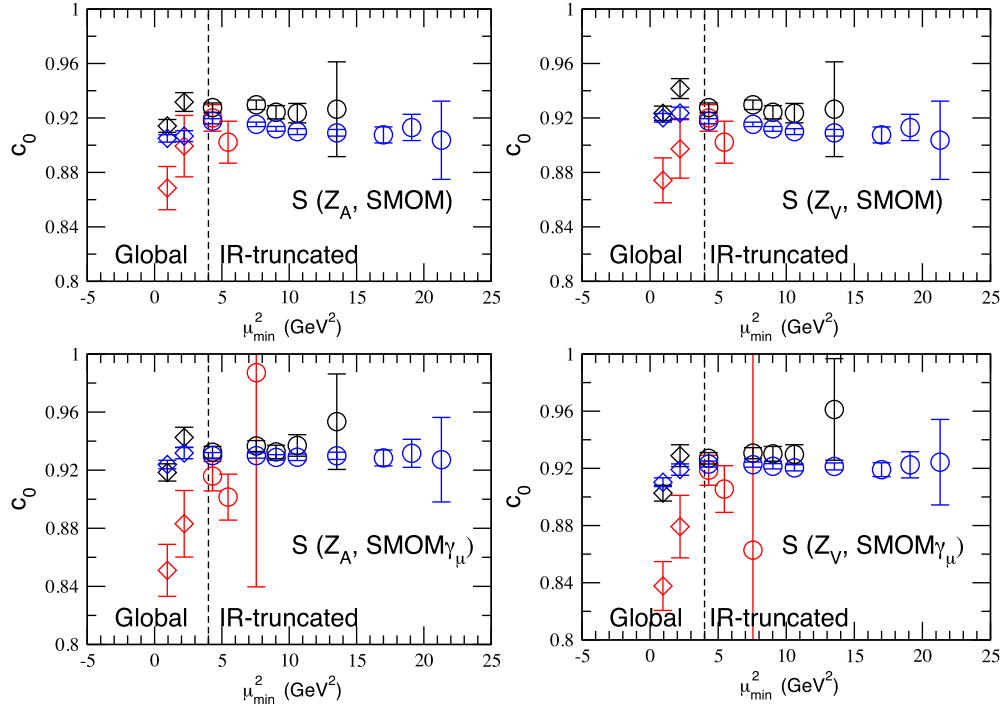
FIG. 6.   Stability test on the μ_0-independent contribution c_0 for the scalar channel with variation of $\mu_{\min}$ under the choices of $\mu_{\max} = 3$ (red), 4 (black), and 5 (blue) GeV. Diamond symbols appearing in the left side of the vertical dashed line are given by the global fit, while circle symbols appearing in the right side of the vertical dashed line are given by the IR-truncated fit results. The choice of $k_{\max} = 2$ is adopted for the polynomial terms in both functional forms used in the global fit and the IR-truncated fit.
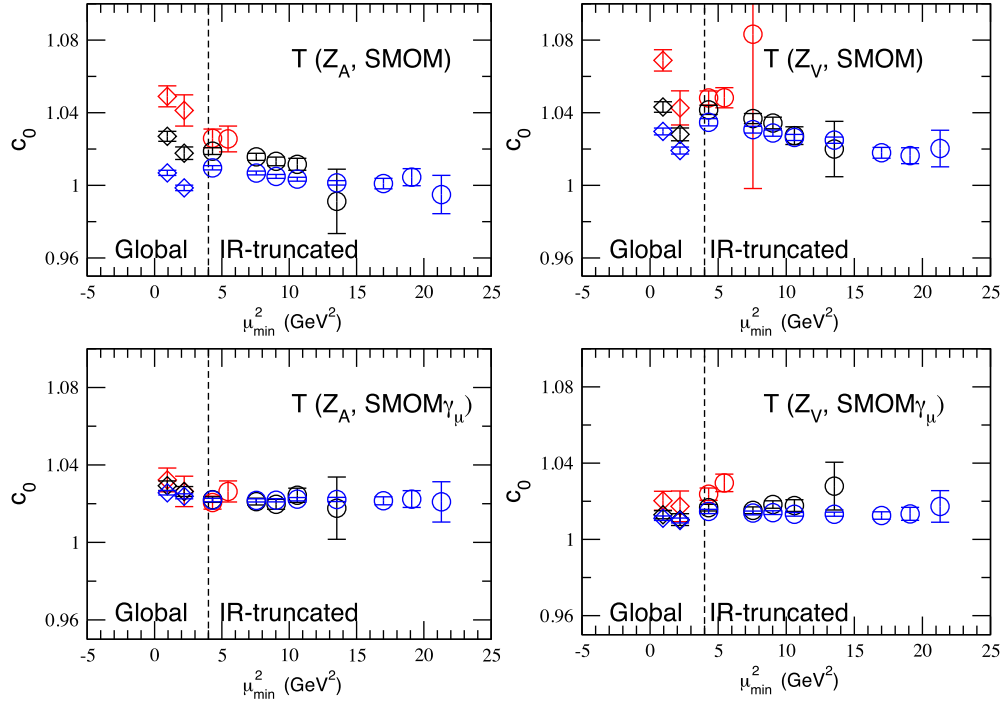

FIG. 7.   Stability test on the μ_0-independent contribution c_0 for the tensor channel with variation of $\mu_{\min}$ under the choices of $\mu_{\max} = 3$ (red), 4 (black), and 5 (blue) GeV. The rest is the same as in Fig. 6.

TABLE V.   Results of the renormalization constants $Z_S^{\overline{\text{MS}}}(2\text{ GeV})$ and $Z_T^{\overline{\text{MS}}}(2\text{ GeV})$ with the RI/SMOM$_{\gamma_\mu}$ intermediate scheme. The obtained values are evaluated by three types of the global fit that satisfy all our guidelines to select the appropriate fit range of $[\mu_{\min}:\mu_{\max}]$ with a smaller value of $k_{\max}$ as discussed in Sec. III C. The first error denotes the statistical one, while the second and third errors represent the systematic uncertainties in the determination of the μ_0-independent contribution as described in the text.

Type	Fit range (GeV)	$k_{\max}$	$Z_S^{\overline{\text{MS}}}(2\text{ GeV})$	χ^2/dof	$Z_T^{\overline{\text{MS}}}(2\text{ GeV})$	χ^2/dof
A	[1:4]	1	0.8966(23)(136)(156)	1.05(34)	1.0143(9)(186)(20)	0.34(13)
B	[1:4]	2	0.9027(55)(207)(243)	1.03(37)	1.0129(21)(303)(37)	0.33(14)
C	[1:5]	2	0.9103(31)(136)(127)	0.92(31)	1.0111(12)(186)(36)	0.30(13)

μ_0-dependences of $Z_S^{\overline{\text{MS}}}(2\text{ GeV})$ and $Z_T^{\overline{\text{MS}}}(2\text{ GeV})$ at higher μ_0 can be well described by a quadratic function of $(a\mu_0)^2$. Furthermore, the resulting c_0 value does not change so much even changing from $\mu_{\max} = 4$ GeV (black symbols) to $\mu_{\max} = 5$ GeV (blue symbols). This suggests that the choice of $k_{\max} = 2$ is enough to cope with the μ_0-dependence appearing at higher μ_0, which is caused by the lattice discretization artifacts, up to $\mu_0 = 5$ GeV. Once the ultraviolet behavior is well controlled by the polynomial terms with the optimal choice of $k_{\max}$, both fit procedures lead to compatible results, especially for the SMOM$_{\gamma_\mu}$ cases as shown in Figs. 6 and 7. We therefore choose the RI/SMOM$_{\gamma_\mu}$ scheme and the SF input of Z_V for evaluating the final results of $Z_S^{\overline{\text{MS}}}(2\text{ GeV})$ and $Z_T^{\overline{\text{MS}}}(2\text{ GeV})$, and also quote the systematic uncertainties (denoted as a subscript of "scheme") which are determined from the maximum difference among the four combinations of {SF input, scheme}.

According to the aforementioned discussion, we consider three types of the choices of $k_{\max}$ and the fit range of $[\mu_{\min}:\mu_{\max}]$ as a candidate of the best choice for the global fit. Our best estimate of $Z_S^{\overline{\text{MS}}}(2\text{ GeV})$ and $Z_T^{\overline{\text{MS}}}(2\text{ GeV})$ obtained from the combination of $\{Z_V, \text{SMOM}_{\gamma_\mu}\}$ are summarized in Table V. The first error denotes the statistical error, while the second error represents the systematic error determined from the maximum difference among the four combinations of {SF input, scheme}. The third error represents the systematic error determined by the size of the deviation from the IR-truncated fit result with the same choice of $k_{\max}$ (denoted as a subscript of "model"). For the tensor case, all results obtained from three different types of the global fit are consistent with each other within their statistical accuracy, while a mutual consistency in the

scalar case is assured if the systematic uncertainties are taken into account. The results from the Type C case have smaller uncertainties on two systematic errors in both the scalar and tensor channels. We therefore choose the results obtained from the Type C case as our central values of $Z_S^{\overline{\text{MS}}}(2\text{ GeV})$ and $Z_T^{\overline{\text{MS}}}(2\text{ GeV})$ and quote the third systematic error that is determined from the maximum difference among above three results (denoted as a subscript of "fit") according to our guidelines in the determination of the μ_0-independent term as discussed in Sec. III C.

Hence, our final results of the renormalization constants for the scalar and tensor current operators are

$$Z_S^{\overline{\text{MS}}}(2\text{ GeV}) = 0.9103(31)_{\text{stat}}(136)_{\text{scheme}}(127)_{\text{model}}(137)_{\text{fit}}$$
$$= 0.9103(31)_{\text{stat}}(231)_{\text{syst}} \qquad (35)$$

$$Z_T^{\overline{\text{MS}}}(2\text{ GeV}) = 1.0111(12)_{\text{stat}}(186)_{\text{scheme}}(36)_{\text{model}}(32)_{\text{fit}}$$
$$= 1.0111(12)_{\text{stat}}(192)_{\text{syst}}. \qquad (36)$$

On these renormalization constants, the error budget is compiled in Table VI. All errors of the renormalization constants become small enough to be comparable to the precision that is reached for the bare couplings with the statistical errors at the 1%–2% level as tabulated in Table IV, since we use the RI/SMOM$_{(\gamma_\mu)}$ intermediate scheme that can considerably reduce the systematic errors compared to the case of the RI/MOM scheme.

C. Renormalized coupling

The renormalized value of the coupling can be evaluated by combining the value of the bare coupling with the renormalization constant as $Z_O \times g_O^{\text{bare}}$. The renormalized couplings g_O for $O = V, A, S, T$ obtained

TABLE VI.   The error budget for $Z_S^{\overline{\text{MS}}}(2\text{ GeV})$ and $Z_T^{\overline{\text{MS}}}(2\text{ GeV})$ with the RI/SMOM$_{\gamma_\mu}$ intermediate scheme.

		Scalar (Z_S)	Tensor (Z_T)
Statistical:		0.34%	0.12%
Systematical:	Choice of scheme ("scheme")	1.49%	1.84%
	Choice of fit model ("model")	1.40%	0.36%
	Variation of fit ("fit")	1.50%	0.32%
Total:		2.56%	1.90%

TABLE VII.   Results of the renormalized couplings g_O for $O = V$, A, S, T obtained from both 128^4 and 64^4 lattices with different choices of the source-sink separation (t_{sep}) and the smearing type. The scalar and tensor couplings (g_S and g_T) are renormalized in the $\overline{\mathrm{MS}}$ scheme at the renormalization scale of $\mu = 2$ GeV. The second errors on g_S and g_T are given by the total systematic uncertainties for the determination of the renormalization constants.

L	t_{sep}	Smearing-type	g_V	g_A	g_S	g_T
128	10	Exp.(I)	0.997(1)	1.276(26)	$0.545(180)_{\mathrm{stat}}(13)_{\mathrm{syst}}$	$1.120(14)_{\mathrm{stat}}(21)_{\mathrm{syst}}$
	12		0.997(2)	1.278(24)	$0.743(134)_{\mathrm{stat}}(17)_{\mathrm{syst}}$	$1.036(22)_{\mathrm{stat}}(20)_{\mathrm{syst}}$
	14		1.000(2)	1.275(38)	$0.950(321)_{\mathrm{stat}}(22)_{\mathrm{syst}}$	$0.988(37)_{\mathrm{stat}}(19)_{\mathrm{syst}}$
	16		0.997(4)	1.309(60)	$0.859(306)_{\mathrm{stat}}(20)_{\mathrm{syst}}$	$1.019(57)_{\mathrm{stat}}(19)_{\mathrm{syst}}$
	13	Gauss	0.998(1)	1.209(34)	$0.713(140)_{\mathrm{stat}}(17)_{\mathrm{syst}}$	$1.044(20)_{\mathrm{stat}}(20)_{\mathrm{syst}}$
	16		0.993(2)	1.267(24)	$0.381(296)_{\mathrm{stat}}(9)_{\mathrm{syst}}$	$0.988(55)_{\mathrm{stat}}(19)_{\mathrm{syst}}$
64	11	Exp.(I)	0.999(7)	1.230(18)	$1.313(380)_{\mathrm{stat}}(31)_{\mathrm{syst}}$	$1.063(21)_{\mathrm{stat}}(20)_{\mathrm{syst}}$
	14		1.010(7)	1.299(35)	$1.055(360)_{\mathrm{stat}}(25)_{\mathrm{syst}}$	$1.013(27)_{\mathrm{stat}}(19)_{\mathrm{syst}}$
	12	Exp.(II)	1.011(13)	1.246(12)	$1.003(116)_{\mathrm{stat}}(23)_{\mathrm{syst}}$	$1.027(9)_{\mathrm{stat}}(20)_{\mathrm{syst}}$
	14		0.997(4)	1.292(15)	$0.972(153)_{\mathrm{stat}}(23)_{\mathrm{syst}}$	$1.054(9)_{\mathrm{stat}}(20)_{\mathrm{syst}}$
	16		0.998(11)	1.263(37)	$1.398(397)_{\mathrm{stat}}(33)_{\mathrm{syst}}$	$0.966(32)_{\mathrm{stat}}(18)_{\mathrm{syst}}$

from both $L = 128$ and $L = 64$ calculations are summarized in Table VII. The scalar and tensor couplings (g_S and g_T) are renormalized in the $\overline{\mathrm{MS}}$ scheme at the renormalization scale of 2 GeV, while the vector and axial-vector couplings are renormalized with $Z_V = 0.95153(76)$ and $Z_A = 0.9650(68)$ obtained with the SF scheme. The jackknife method is used to estimate the statistical error. For the scalar and tensor couplings, both the statistical and systematic errors are quoted. The systematic error stems from the determination of the renormalization constant in the Rome-Southampton method as discussed in Sec. III C.

1. Axial-vector couplings

Figure 8 shows t_{sep} dependence on the renormalized value of the axial-vector coupling g_A. In the case of the exponential smeared source, our results of g_A obtained with $t_{\mathrm{sep}} = \{12, 14, 16\}$ for the $L = 128$ lattice and with $t_{\mathrm{sep}} = \{14, 16\}$ for the $L = 64$ lattice agree well with the experimental value, 1.2754(13) [52], while only one result obtained with $t_{\mathrm{sep}} = 16$ for the Gaussian smeared source can reproduce the experimental value. The latter smearing results are only obtained with two different values of t_{sep}, so that the details of t_{sep} dependence are not clear. However, at least, the condition of $t_{\mathrm{sep}} \geq 14$, corresponding to $t_{\mathrm{sep}} \gtrsim 1.2$ fm, is large enough to eliminate the excited-state contaminations regardless of the smearing type that we used in this study. In addition, it is certainly confirmed that systematic uncertainties stemming from the finite-size effect are negligible at the level of the statistical precision of 1.9% in two large spatial extents of about 10 and 5 fm.

Taking into account these observations, we determine the central value of g_A from several combinations that can be made by selecting the dataset and imposing restrictions on t_{sep}. In Table VIII, we list four different combined results by using only data calculated with the exponential smeared source. The listed mean values are first computed by a weighted average of the selected data with a covariance matrix accounting for correlation on each lattice ensemble. As for the combined analysis with both 128^4 and 64^4 lattices, we simply take an average of two combined results obtained from both 128^4 and 64^4 lattices with respect to their statistical uncertainties, which are evaluated by the
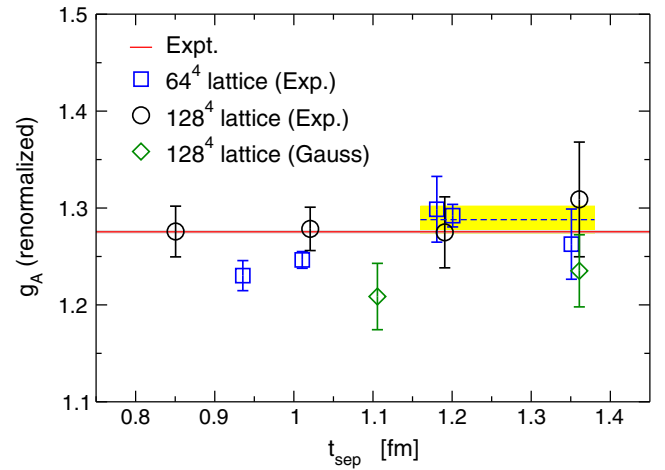

FIG. 8. t_{sep} dependence of the renormalized values of g_A. The horizontal axis denotes the source-sink separation t_{sep} in physical unit. Square symbols for the $L = 64$ calculations have been slightly shifted in horizontal direction if they need to avoid overlap. The solid line denotes the experimental value, while the dotted line represents the average value, and shaded band displays the fit range and one standard deviation.

TABLE VIII. Results of the renormalized couplings, g_A, g_S, and g_T from the combined analysis with different data selections for lattice volumes and t_{sep}.

Dataset	t_{sep}	# of data	g_A	g_S	g_T
64^4	$\{14, 16\}$	3	1.288(16)	$1.021(142)_{stat}(24)_{syst}$	$1.042(9)_{stat}(20)_{syst}$
128^4 (only Exp.)	$\{12, 14, 16\}$	3	1.280(24)	$0.767(141)_{stat}(18)_{syst}$	$1.020(22)_{stat}(20)_{syst}$
$64^4 + 128^4$ (only Exp.)	$\{14, 16\}$	5	1.288(14)	$0.894(100)_{stat}(21)_{syst}$	$1.038(9)_{stat}(20)_{syst}$
$64^4 + 128^4$ (only Exp.)	$\{12, 14, 16\}$	7	1.267(12)	$0.927(83)_{stat}(22)_{syst}$	$1.036(6)_{stat}(20)_{syst}$

jackknife method.[5] Although inclusion of the data obtained with $t_{sep} = 12$ in the $L = 64$ calculations slightly reduces the mean value, all four results are in good agreement with each other. We prefer to choose the combined value of g_A with $t_{sep} = \{14, 16\}$ from both $L = 128$ and $L = 64$ calculations as our best estimate of g_A.

Our final result of g_A in this study is

$$g_A = 1.288(14)_{stat}(9)_{Z_A}, \tag{37}$$

where we also include a systematic error stemming from the error of Z_A^{SF}. This result reproduces the experimental value at the precision level of 1%.

2. Scalar and tensor couplings

In Fig. 9, we show the results for the renormalized values of g_S (left) and g_T (right), which are obtained with several different choices of t_{sep} on two lattice volumes. In both cases of g_S and g_T, there is no distinct t_{sep} dependence in the region of $t_{sep} \geq 12$, corresponding to $t_{sep} \gtrsim 1.0$ fm.[6] This observation ensures that systematic uncertainties stemming from the excited-state contaminations are well under control for $t_{sep} \geq 12$ with both smeared methods. Therefore, similar to the case of g_A, we get the combined results obtained from four types of data selection as summarized in Table VIII. All four results of g_T are fairly consistent with each other, while the scalar case shows a rough consistency within the larger statistical errors. We then choose the combined values of g_S and g_T with $t_{sep} = \{12, 14, 16\}$ from both $L = 128$ and $L = 64$ calculations. As will be discussed in Appendix D, the values of g_S and g_T determined by the summation method with datasets of $t_{sep} = \{12, 14, 16\}$ are barely consistent with the above estimations, though the results from the summation method are much larger uncertainties than those of the plateau method. Furthermore, the two-state fit analysis, which is

only applied to g_T, does not lead to a major discrepancy beyond the statistical precision.

Our best estimates are

$$g_S = 0.927(83)_{stat}(22)_{Z_S} \quad \text{and} \quad g_T = 1.036(6)_{stat}(20)_{Z_T}, \tag{38}$$

where the second errors are given by the total systematic uncertainties for the determination of the renormalization constants.

We finally compare our results of the renormalized values of g_S (left) and g_T (right) together with results from the recent lattice QCD calculations [11–20] in Fig. 10. Remark that our results are obtained solely from the physical point simulations which suffer from large statistical fluctuations, while the other lattice results are given by the combined data that includes the data taken from simulations at the heavier pion masses. However, the statistical and total errors on our results are comparable to the other lattice results, since we use the AMA method for the bare matrix elements and the RI/SMOM$_{(\gamma_\mu)}$ scheme for the renormalization, both of which reduce the statistical and systematic uncertainties on the final results. As for g_S, our result is consistent with the trend of the other results. On the other hand, our result of g_T locates slightly higher than other continuum results (green labels), though this discrepancy would be caused by the discretization uncertainty that is not yet accounted in our calculations.

VI. SUMMARY

We have calculated the renormalized values of the nucleon isovector-couplings in the axial-vector, scalar and tensor channels using $2 + 1$ flavor lattice QCD with physical light quarks. The calculations are carried out with the gauge configurations generated by the PACS Collaboration with the stout-smeared $O(a)$ improved Wilson quark action and Iwasaki gauge action [39] at a single lattice spacing of $a \approx 0.085$ fm on the two lattice volumes (linear spatial extents of 10.9 fm and 5.5 fm). In order to achieve high-precision and high-accuracy determination, we employ the AMA technique which can reduce the statistical error significantly, and the RI/SMOM$_{(\gamma_\mu)}$

---

[5]We also perform the super-jackknife analysis [53,54], but the results mostly remain same within their errors since the $L = 128$ and $L = 64$ lattice ensembles are independent.

[6]Here, it is worth mentioning that the choice of the wider range of t_{sep} than that of g_A is based on the fact that two results from the Gaussian smeared source with $t_{sep} = \{13, 16\}$ are consistent within the statistical errors for g_S and g_T.
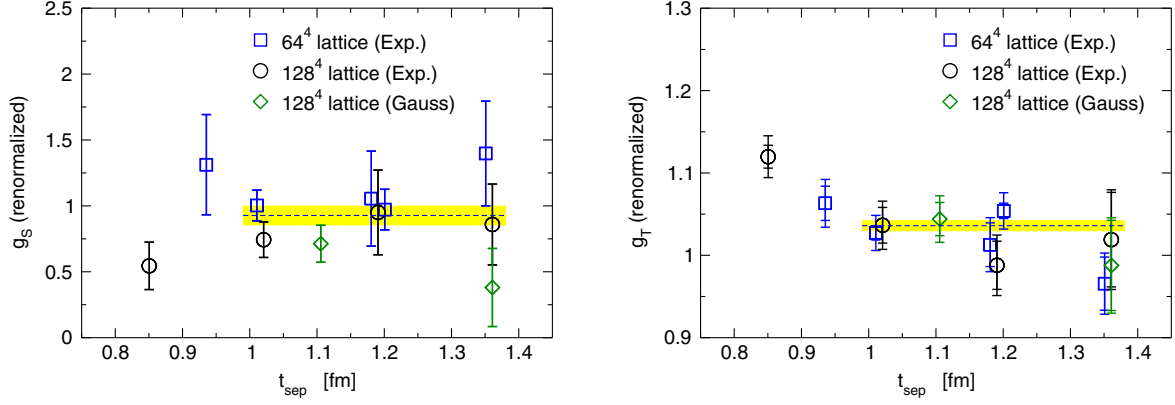
FIG. 9. t_{sep} dependence of the renormalized values of g_S (left) and g_T (right). The horizontal axis denotes the source-sink separation t_{sep} in physical unit. The inner and outer error bars represent their statistical and total uncertainties, respectively. The rest is the same as in Fig. 8.

scheme which keeps the systematic error under control in the determination of $Z_S^{\overline{\text{MS}}}(2 \text{ GeV})$ and $Z_T^{\overline{\text{MS}}}(2 \text{ GeV})$.

We have confirmed that systematic uncertainties stemming from the finite-size effects are negligible in two large spatial extents of about 10 and 5 fm. The effects of the excited-state contamination have also been investigated by varying t_{sep} from 0.85 to 1.36 fm in the standard plateau method. It was found that the condition of $t_{\text{sep}} \gtrsim 1.0$ fm for g_S and g_T is large enough to eliminate the excited-state contaminations thanks to the elaborated tuning of the sink and source functions, while the condition of $t_{\text{sep}} \gtrsim 1.2$ fm is required for g_A. Taking account of the uncertainties stemming from the excited-state contamination, our best estimates for the nucleon isovector couplings, g_A, g_S, and g_T are obtained as follows:

$$g_A = 1.288(14)(9) \tag{39}$$

$$g_S = 0.927(83)(22) \tag{40}$$

$$g_T = 1.036(6)(20), \tag{41}$$

where the first error is statistical, while the second one represents a systematic error given by the total uncertainties in the determination of the renormalization constant. Our result of g_A is fairly consistent with the experimental result at a percent level of accuracy ($\Delta g_A / g_A \sim 1\%$). For g_S and g_T, our results are consistent with those of the FLAG average [11], though the discretization uncertainty is not yet accounted in this study. It is worth remarking that our
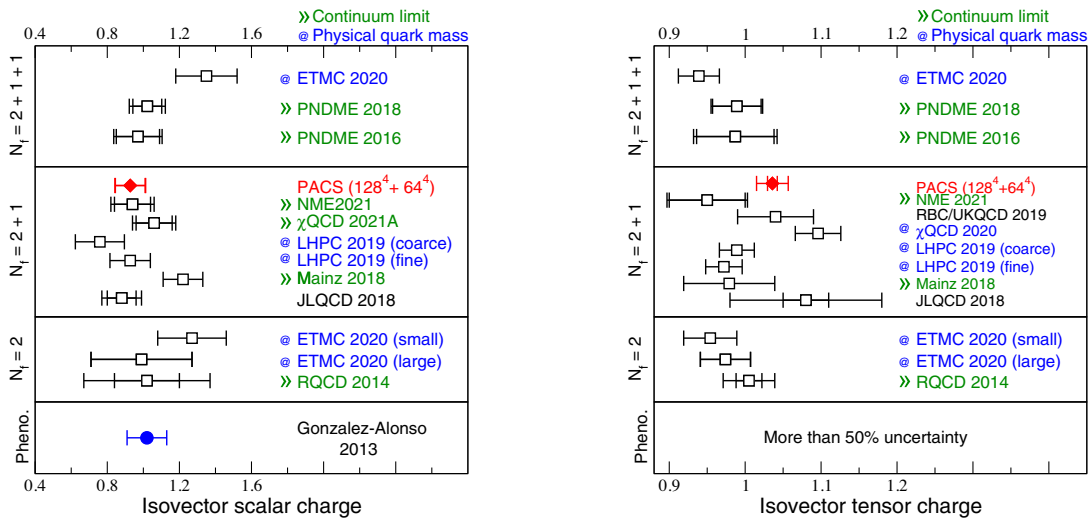

FIG. 10.   Comparison of our results (red diamonds) with the other lattice results (black squares) [11–20] and the phenomenological value (blue circle) [6] for g_S (left panel) and g_T (right panel). The inner error bars represent the statistical uncertainties, while the outer ones represent the total uncertainties given by adding the statistical and systematic errors in quadrature. Blue labels indicate that the analysis includes the data from lattice QCD simulation near the physical point, while green labels indicate that the continuum extrapolation is achieved.

preliminary result of g_A/g_V obtained at a second, finer lattice spacing ($a \approx 0.063$ fm) shows a very small discretization error on g_A/g_V at the lattice spacing of $a \approx 0.085$ fm [55]. The overall uncertainties on our results of g_S and g_T determined directly at the physical point reach $\Delta g_S/g_S \sim 8\%$ and $\Delta g_T/g_T \sim 2\%$, which are smaller than the FLAG average for both $N_f = 2 + 1 + 1$ ($\Delta g_S/g_S \sim 10\%$ and $\Delta g_T/g_T \sim 3\%$) and $N_f = 2 + 1$ ($\Delta g_S/g_S \sim 12\%$ and $\Delta g_T/g_T \sim 6\%$) [11].

We continue our research to evaluate the systematic uncertainties of g_S and g_T due to the discretization error, using the PACS10 gauge configurations at the finer lattice spacing of $a \approx 0.063$ fm at the physical point. We also plan to extend to investigate individual components of g_O^u, g_O^d, and g_O^s for $O = A$, S, T, which demand calculations of the disconnected contribution of the nucleon 3-point correlation functions. Further study is now in progress [55].

APPENDIX A: COMPARISON BETWEEN THE RI/MOM AND RI/SMOM$_{(\gamma_\mu)}$ SCHEMES

It was reported in Ref. [31] that the RI/SMOM$_{(\gamma_\mu)}$ scheme significantly reduces sensitivity to the unwanted infrared divergence, which stems from the nonperturbative effects such as the spontaneous chiral symmetry breaking. It is simply because the nonexceptional momenta ($p_1^2 = p_2^2 = q^2$) can avoid contributions from the nonperturbative effects due to the nonvanishing value of q^2. Furthermore, the better convergence of the perturbative series for the matching from RI/SMOM$_{(\gamma_\mu)}$ to $\overline{\text{MS}}$ was observed for the case of the mass renormalization Z_m [32] and it has been confirmed that this trend is maintained up to the two-loop level [33,56]. Recall that $Z_m = 1/Z_P$ is satisfied in the RI/SMOM$_{(\gamma_\mu)}$ scheme [32], while the good chiral property leads to the relation of $Z_S = Z_P$ in the massless limit. In this context, the RI/SMOM$_{(\gamma_\mu)}$ scheme is expected to provide better estimation of the renormalization constant for the scalar channel Z_S with reduced systematic uncertainties.

In this calculation, we use the quark propagator calculated with a single source location $x_0 = (0, 0, 0, 0)$, while the SMOM$_{(\gamma_\mu)}$ results are obtained with four different source locations as described in Sec. V B.

Figure 11 shows the renormalization constants $Z_S^{\overline{\text{MS}}}(2 \text{ GeV})$ (upper panels) and $Z_T^{\overline{\text{MS}}}(2 \text{ GeV})$ (lower panels) obtained from the RI/MOM intermediate scheme as a function of the square of the matching scale μ_0. The SF input of Z_A is adopted in the left panels, while Z_V is used for the right panels. In each panel of Fig. 11, red and blue curves with error bands represent two fit results from the global fit (28) with $\mu_{\min} = 1$ GeV and the IR-truncated fit (29) with $\mu_{\min} = 2$ GeV under the conditions of $k_{\max} = 2$ and $\mu_{\max} = 5$ GeV, while green curve with error bands is given by removing the divergent contribution from the global fit result. The intersections of the green and blue curves with the y-axis correspond to the μ_0-independent contributions in the global fit (28) and the IR-truncated fit (29). Their central values and statistical errors denoted as the circle and squared symbols are slightly shifted from the y-axis in each panel of Fig. 11 similar to those shown in Figs. 4 and 5.

As clearly displayed in the upper panels of Fig. 11, the μ_0-independent value of $Z_S^{\overline{\text{MS}}}(2 \text{ GeV})$ is severely infrared sensitive compared to the case of the RI/SMOM$_{(\gamma_\mu)}$ scheme. On the other hand, as for the tensor channel displayed in the lower panels of Fig. 11, the μ_0-independent value of $Z_S^{\overline{\text{MS}}}(2 \text{ GeV})$ obtained from the RI/MOM scheme equally shows less sensitivity to the unwanted infrared divergence as well as the RI/SMOM$_{(\gamma_\mu)}$ scheme, since the tensor channel is not strongly affected by the spontaneous chiral symmetry breaking.

Finally, similar to the case of SMOM$_{(\gamma_\mu)}$, we choose the global fit results for the central value of $Z_S^{\overline{\text{MS}}}(2 \text{ GeV})$ and $Z_T^{\overline{\text{MS}}}(2 \text{ GeV})$ obtained from the RI/MOM intermediate scheme as summarized in Table IX. The first, second and third errors are the statistical one and the systematic ones associated with "scheme" and "model". The third error caused by choice of fit model is the largest of the three
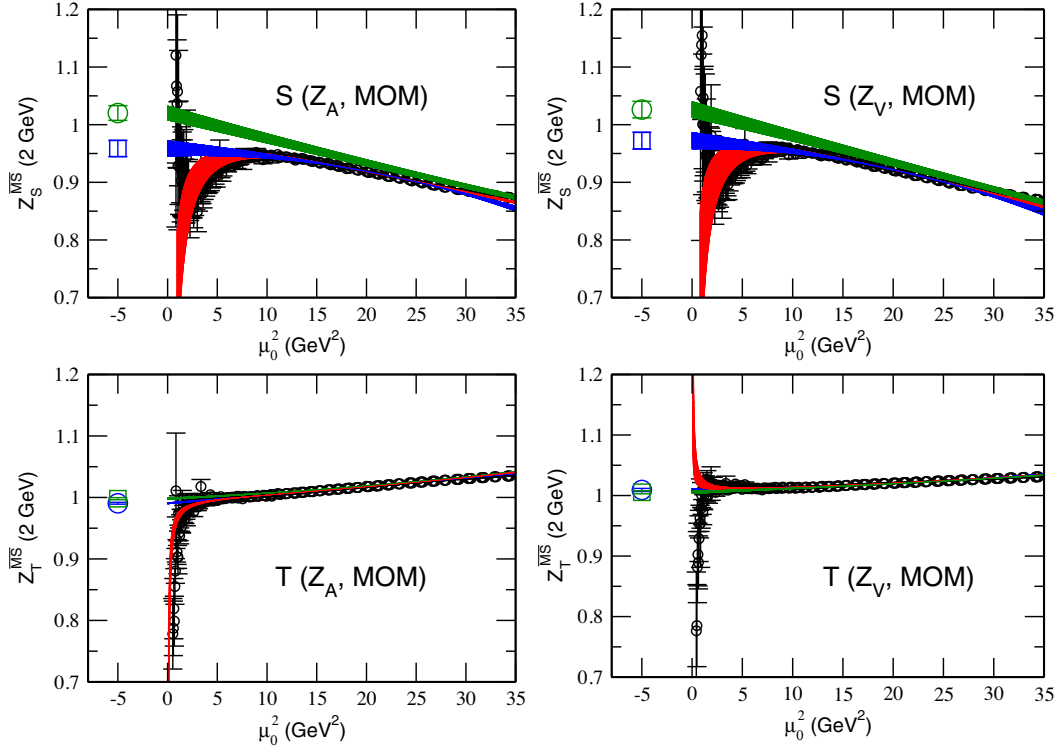
FIG. 11.   The renormalization constants of $Z_S^{\overline{\mathrm{MS}}}(2\text{ GeV})$ (upper panels) and $Z_T^{\overline{\mathrm{MS}}}(2\text{ GeV})$ (lower panels) obtained from the RI/MOM scheme as a function of the square of the matching scale μ_0. The SF input of Z_A is used for the left panels, while the SF input of Z_V is used for the right panels. The rest is the same as in Figs. 4 and 5.

errors and its size is about a few times its own statistical accuracy. Especially, this largest error on $Z_S^{\overline{\mathrm{MS}}}(2\text{ GeV})$ from the MOM case is much larger than that of the SMOM$_{(\gamma_\mu)}$ case due to more significant sensitivity to the unwanted infrared divergence. Therefore, we confirm that the RI/SMOM$_{(\gamma_\mu)}$ scheme can provide better estimation of the renormalization constant with reduced sensitivity to the unwanted infrared divergence compared to the RI/MOM scheme.

APPENDIX B: TRUNCATION ERRORS OF THE PERTURBATIVE SERIES IN MATCHING AND EVOLUTION

As described in Sec. III, we first determine the renormalization constant Z_O^{RI} for the O channel in one of three RI schemes in a fully nonperturbative way. The obtained value of Z_O^{RI} is converted and evolved to the $\overline{\mathrm{MS}}$ scheme at the renormalization scale of 2 GeV with the help of perturbation theory. Therefore, it is inevitable that there are

TABLE IX.   Results of the renormalization constants $Z_S^{\overline{\mathrm{MS}}}(2\text{ GeV})$ and $Z_T^{\overline{\mathrm{MS}}}(2\text{ GeV})$ from the RI/MOM scheme using the global fit of the Type C.

Scheme	Fit range (GeV)	$k_{\max}$	$Z_S^{\overline{\mathrm{MS}}}(2\text{ GeV})$	χ^2/dof	$Z_T^{\overline{\mathrm{MS}}}(2\text{ GeV})$	χ^2/dof
MOM	[1:5]	2	0.9723(148)(136)(539)	1.13(52)	1.0092(25)(38)(62)	0.45(13)

TABLE X.   List of three types of perturbative conversion to $\overline{\mathrm{MS}}$ at the scale of 2 GeV.

	LO	NLO	NNLO
Scheme matching from RI/SMOM$_{(\gamma_\mu)}$ to $\overline{\mathrm{MS}}$	Tree	1-loop	2-loop
Scale evolution in $\overline{\mathrm{MS}}$ (anomalous dim.)	1-loop	2-loop	3-loop
Scale evolution in $\overline{\mathrm{MS}}$ (running coupling α_s)	4-loop	4-loop	4-loop

TABLE XI. Results of the renormalization constants $Z_S^{\overline{\mathrm{MS}}}(2\text{ GeV})$ and $Z_T^{\overline{\mathrm{MS}}}(2\text{ GeV})$ from the RI/SMOM$_{\gamma_\mu}$ with the LO, NLO, and NNLO conversion factors using the global fit of the Type C. The first, second, third, and fourth errors represent the statistical one and the systematic ones associated with "scheme," "model," and "fit," respectively.

	FIT range (GeV)	$k_{\max}$	$Z_S^{\overline{\mathrm{MS}}}(2\text{ GeV})$	$Z_T^{\overline{\mathrm{MS}}}(2\text{ GeV})$
LO	[1:5]	2	0.8982(27)(431)(358)(154)	0.9726(11)(497)(193)(33)
NLO	[1:5]	2	0.9045(30)(130)(1)(130)	1.0109(12)(265)(53)(31)
NNLO	[1:5]	2	0.9103(31)(53)(73)(137)	1.0111(12)(149)(20)(32)

truncation errors of the perturbative series in matching and evolution. To examine the size of such systematic uncertainties, we compare the values of Z_O^{RI} using three different types of perturbative conversion as listed in Table X.

For the case of the RI/SMOM$_{\gamma_\mu}$ intermediate scheme, we evaluate $Z_S^{\overline{\mathrm{MS}}}(2\text{ GeV})$ and $Z_T^{\overline{\mathrm{MS}}}(2\text{ GeV})$ with the leading order (LO), the next-to-leading order (NLO) and NNLO conversion factors as tabulated in Table XI. The first, second, third and fourth errors represent the statistical one and the systematic ones associated with "scheme," "model," and "fit," respectively. As mentioned in Sec. III B 3, we assume that the systematic error associated with scheme can be regarded as possible truncation errors in perturbation matching and evolution.

We indeed observe that the difference between the NLO and NNLO results is sufficiently small compared to the difference between the LO and NNLO results in Table X. For the case of the scalar, the size of the truncation error from NLO to NNLO in perturbation theory is comparable to the systematic error associated with scheme, while such perturbation truncation error is negligible for the case of the tensor in comparison to any other systematic uncertainties.

APPENDIX C: THE QCD RUNNING OF α_s AND PERTURBATIVE MATCHING FOR Z_O

The QCD running coupling $\alpha_s(\mu)$ is determined by the renormalization group equation. To calculate the coupling constant $\alpha_s = g^2/4\pi$ at any scale, we used the four-loop (NNNLO) running formula:

$$
\begin{aligned}
\frac{da_s}{d\ln\mu^2} &= -\sum_{n=0}^{\infty}\beta_n(a_s)^{n+2} \\
&= -\beta_0 a_s^2 - \beta_1 a_s^3 - \beta_2 a_s^4 - \beta_3 a_s^5 + \mathcal{O}(a_s^6), \quad (\text{C1})
\end{aligned}
$$

where $a_s = \alpha_s/4\pi$ using the four-loop QCD beta function which was calculated in Ref. [57].

For a numerical implementation, the methodology described in Ref. [31] is employed in this work. The initial condition of the running coupling is given at the scale of $\mu = M_Z$ with the world-average Z-boson mass of 91.1876(21) GeV [52] as below,

$$
\alpha_s^{(5)}(M_Z) = 0.1176 \pm 0.0011, \quad (\text{C2})
$$

where the number in superscript brackets indicates the number of dynamical quarks. While the scale in α_s runs across the m_b and m_c threshold, where each flavor quark is decoupled at its mass scale, the following matching conditions are imposed as

$$
\alpha_s^{(5)}(m_b) = \alpha_s^{(4)}(m_b) \quad \text{and} \quad \alpha_s^{(4)}(m_c) = \alpha_s^{(3)}(m_c). \quad (\text{C3})
$$

Once $\alpha_s^{(3)}(m_c)$ is computed, we can calculate the value of the running coupling $\alpha_s(\mu)$ at any scale in the 3-flavor theory. For example, in this study, we use

$$
\alpha_s^{(3)}(2\text{ GeV}) = 0.2904. \quad (\text{C4})
$$

After performing the conversion from the intermediate renormalization scheme to the $\overline{\mathrm{MS}}$ scheme, we can evaluate the renormalization constant for the quark bilinear operator $Z_O(\mu)$ at any scale. The renormalization group equation is given as

$$
\frac{\partial \ln Z_O}{\partial \ln \mu^2} = \gamma_O = -\sum_{n=0}^{\infty}\gamma_O^{(n)}\left(\frac{\alpha_s}{4\pi}\right)^{n+1}, \quad (\text{C5})
$$

where $\gamma^{(n)}$ represents the n-loop anomalous dimension. For the case of $O = S$ and T, these are evaluated up to two-loop order [33]. In order to compare with the experimental values or other lattice results, we choose the renormalization scale $\mu = 2$ GeV, and then use the evolution factor from the matching scale μ_0 to 2 GeV, $R_O(2\text{ GeV}, \mu_0) = Z_O^{\overline{\mathrm{MS}}}(2\text{ GeV})/Z_O^{\overline{\mathrm{MS}}}(\mu_0)$, which is given as the NNLO accuracy:

$$
\begin{aligned}
&\frac{Z_O^{\overline{\mathrm{MS}}}(2\text{ GeV})}{Z_O^{\overline{\mathrm{MS}}}(\mu_0)} \\
&= \left(\frac{\alpha_s(2\text{ GeV})}{\alpha_s(\mu_0)}\right)^{\frac{\gamma_O^{(0)}}{\beta_0}} \exp\left(\frac{\alpha_s(2\text{ GeV})}{4\pi} - \frac{\alpha_s(\mu_0)}{4\pi}\right)^{\left\{\frac{\gamma_O^{(1)}}{\beta_0} - \frac{\gamma_O^{(0)}\beta_1}{\beta_0^2}\right\}} \\
&\times \exp\left\{\left(\frac{\alpha_s(2\text{ GeV})}{4\pi}\right)^2 - \left(\frac{\alpha_s(\mu_0)}{4\pi}\right)^2\right\}^{\frac{1}{2}\left\{\frac{\gamma_O^{(2)}}{\beta_0} - \frac{\gamma_O^{(1)}\beta_1}{\beta_0^2} - \frac{\gamma_O^{(0)}\beta_2}{\beta_0^2} + \frac{\gamma_O^{(0)}\beta_1^2}{\beta_0^3}\right\}} \\
&\times \exp\{\mathcal{O}(\alpha_s^3)\}. \quad (\text{C6})
\end{aligned}
$$

TABLE XII. Summation method results of the bare couplings g_O for $O = V, A, S, T$ obtained from both 128^4 and 64^4 lattices with available source-sink separations. The smearing-type is chosen to be Exp.(I) for the $L = 128$ calculation and Exp.(II) for the $L = 64$ calculation.

L	Smearing-type	t_{sep}	g_V^{bare}	g_A^{bare}	g_S^{bare}	g_T^{bare}
128	Exp.(I)	$\{10, 12, 14, 16\}$	1.052(5)	1.298(144)	1.138(887)	0.872(88)
64	Exp.(II)	$\{12, 14, 16\}$	1.034(34)	1.517(89)	1.030(882)	1.073(57)

APPENDIX D: ASSESSMENT OF EXCITED-STATE CONTAMINATION

1. Summation method

In this study, we mainly adopted the standard plateau method to determine the bare coupling directly from the ratio (14) as described in Sec. II B. In order to eliminate the systematic uncertainties stemming from the excited-state contaminations, one should calculate the ratio (14) with several choices of t_{sep}, and then make sure whether the evaluated value of the bare coupling does not change with a variation of t_{sep} within a certain precision. Alternatively, there is another method called the summation method, which was proposed to extract the bare coupling from the ratio (14) with a better control of the excited-state contamination [58]. In this method, the ratio of $R(t_{\text{op}}, t_{\text{sep}})$ defined in Eq. (14) is summed over the range of $t_{\text{sink}} > t_{\text{op}} > t_{\text{src}}$ as

$$S(t_{\text{sep}}) = \sum_{t_{\text{op}}=t_{\text{src}}+1}^{t_{\text{sink}}-1} R(t_{\text{op}}, t_{\text{sep}})$$

$$= C + g_O \cdot t_{\text{sep}} + \mathcal{O}(e^{-\Delta E t_{\text{sep}}}), \qquad \text{(D1)}$$

where C is a constant being independent of t_{sep}. The bare coupling g_O can be read off from the slope of $S(t_{\text{sep}})$ with respect to t_{sep}. When more than three sets of t_{sep} are carried out in the plateau method, one can also perform the summation method as well.

The summation method takes an advantage for reducing the excited-state contamination, compared to the plateau method that receives $\mathcal{O}(e^{-\Delta E t_{\text{sep}}/2})$ at most (even when t_{op} is chosen to be right in the middle of the nucleon source and sink operators). However, in general, the summation method requires *various choices* of the source-sink separation t_{sep} to determine the value of g_O by a linear fit as a function of t_{sep} with *smaller uncertainties*. We calculate the nucleon 3-point functions using the sequential source method with a fixed source location [27,50]. Therefore, the number of available data of t_{sep} is quite limited in this study.

The summation method is then applied for both 128^4 and 64^4 lattices with four data sets of $t_{\text{sep}} = \{10, 12, 14, 16\}$ with the smearing-type of Exp.(I) for the former and three datasets of $t_{\text{sep}} = \{12, 14, 16\}$ with the smearing-type of

Exp.(II) for the latter. We then use an uncorrelated linear fit to determine the coupling constant from the slope of the linear dependence of t_{sep} in Eq. (D1). Because of a small number of choices with respect to t_{sep}, the resulting values of the bare coupling as tabulated in Table XII, receive much larger statistical uncertainties than the corresponding values determined by the plateau method. Indeed, no statistically significant results for the scalar channel were obtained from the summation method with both 128^4 and 64^4 lattices.

The consistency between the 128^4 and 64^4 results is clearly seen in the case of the vector channel. These values are fully consistent with the results obtained by the plateau method as listed in Table IV. On the other hand, for the axial-vector and tensor channels, there are some discrepancies between the 128^4 and 64^4 results beyond the statistical errors. It is worth remembering that the plateau method does not show any difference between the 128^4 and 64^4 results of g_A and g_T with high precision. This observation suggest that the discrepancies found in the case of g_A and g_T are mainly caused by rather large uncertainties in the summation method due to fewer choices of t_{sep}. Indeed, in the case of the axial-vector channel, the trend of two data in the $L = 64$ calculations at $t_{\text{sep}} = 12$ and 14, whose statistical errors are much smaller than that of $t_{\text{sep}} = 16$, has a strong influence on the results of the linear fit in the summation method with fewer choices of t_{sep}. Nevertheless, the maximum difference between the plateau and summation methods is less than twice of the standard deviation. In this sense, we confirm that the bare couplings of g_V, g_A, and g_T obtained from both methods are barely consistent with each other.

2. Two-state fit analysis

Although the two analyses with the plateau method and summation method do not lead to major discrepancies in all channels, one may still have concerns about the tensor coupling, which exhibits curvature beyond the statistical errors in Figs. 1 and 2 unlike the other couplings. Therefore, we additionally perform the two-state fit analysis to extract the bare value of g_T from $R(t_{\text{op}}, t_{\text{sep}})$ with the following functional form:

$$R(t'_{\text{op}}, t_{\text{sep}}) = g_T + A \cosh\left[\Delta E\left(t'_{\text{op}} - \frac{t_{\text{sep}}}{2}\right)\right], \qquad \text{(D2)}$$

TABLE XIII.   Two-state fit results of the bare couplings g_T obtained from both 128^4 and 64^4 lattices with smearing-types of Exp.(I) and Exp.(II).

L	t_{sep}	Smearing-type	g_T^{bare}	A	ΔE	Fit-range	χ^2/dof
128	10	Exp.(I)	1.040(36)	0.025(17)	0.55(12)	[1, 9]	0.94
	12		1.015(49)	0.016(49)	0.59(63)	[3, 9]	1.91
	14		0.953(54)	0.004(19)	0.89(113)	[4,10]	0.45
	16		1.020(63)	0.0003(36)	0.84(179)	[3,13]	0.91
64	11	Exp.(I)	1.037(25)	0.0095(93)	0.74(21)	[2, 9]	0.78
	14		0.934(84)	0.051(71)	0.35(18)	[2,11]	1.19
	12	Exp.(II)	0.975(31)	0.035(28)	0.47(15)	[3, 9]	0.51
	14		0.999(23)	0.020(15)	0.46(12)	[3,11]	1.29
	16		0.818(178)	0.012(16)	0.24(13)	[2,14]	0.65

where $t'_{\text{op}} = t_{\text{op}} - t_{\text{src}}$. In this formula, the excited-state contribution remains at most as the size of A at the center of the source and sink operators $t'_{\text{op}} = t_{\text{sep}}/2$. Therefore, the value of A corresponds to a typical size of the systematic uncertainty associated with the excited-state contamination in the plateau method.

The two-state fit results for the bare couplings g_T are summarized in Table XIII. Although the results of g_T^{bare} from the two-state fit analysis are slightly smaller than those of the plateau method, the size of the corresponding correction due to nonzero value of A is a few percent level in each case, but statistically not so significant. If we choose datasets of $t_{\text{sep}} = \{12, 14, 16\}$ from both $L = 128$

and $L = 64$ calculations, we evaluate the average value of the renormalized coupling g_T from the combined analysis using the super-jackknife method as

$$g_T = 0.999(45) \tag{D3}$$

which is consistent with that of the plateau method within the statistical error. This observation indicates that systematic uncertainties stemming from the excited-state contamination are well under control within the limits of the statistical precision thanks to the optimal choice of the smearing parameters used in this study.

[1] P. Herczeg, Prog. Part. Nucl. Phys. **46**, 413–457 (2001).

[2] A. Czarnecki, W. J. Marciano, and A. Sirlin, Phys. Rev. Lett. **120**, 202002 (2018).

[3] T. Bhattacharya, V. Cirigliano, S. D. Cohen, A. Filipuzzi, M. Gonzalez-Alonso, M. L. Graesser, R. Gupta, and H. W. Lin, Phys. Rev. D **85**, 054512 (2012).

[4] V. Cirigliano, S. Gardner, and B. Holstein, Prog. Part. Nucl. Phys. **71**, 93 (2013).

[5] M. González-Alonso, O. Naviliat-Cuncic, and N. Severijns, Prog. Part. Nucl. Phys. **104**, 165–223 (2019).

[6] M. González-Alonso and J. Martin Camalich, Phys. Rev. Lett. **112**, 042501 (2014).

[7] J. D. Jackson, S. B. Treiman, and H. W. Wyld, Phys. Rev. **106**, 517 (1957).

[8] Y. Grossman, Y. Nir, and R. Rattazzi, Adv. Ser. Dir. High Energy Phys. **15**, 755 (1998).

[9] A. Courtoy, S. Baeßler, M. González-Alonso, and S. Liuti, Phys. Rev. Lett. **115**, 162001 (2015).

[10] H. W. Lin, W. Melnitchouk, A. Prokudin, N. Sato, and H. Shows, Phys. Rev. Lett. **120**, 152502 (2018).

[11] Y. Aoki, T. Blum, G. Colangelo, S. Collins, M. Della Morte, P. Dimopoulos, S. Dürr, X. Feng, H. Fukaya, M. Golterman *et al.*, Eur. Phys. J. C **82**, 869 (2022).

[12] S. Park , R. Gupta, B. Yoon, S. Mondal, T. Bhattacharya, Y.-C. Jang, B. Joó, and F. Winter (Nucleon Matrix Elements (NME) Collaboration), Phys. Rev. D **105**, 054505 (2022).

[13] D. Horkel, Y. Bi, M. Constantinou, T. Draper, J. Liang, K.-F. Liu, Z. Liu, and Y.-B. Yang (χQCD Collaboration), Phys. Rev. D **101**, 094501 (2020).

[14] R. Gupta, Y. C. Jang, B. Yoon, H. W. Lin, V. Cirigliano, and T. Bhattacharya, Phys. Rev. D **98**, 034503 (2018).

[15] T. Bhattacharya, V. Cirigliano, S. Cohen, R. Gupta, H. W. Lin, and B. Yoon, Phys. Rev. D **94**, 054508 (2016).

[16] C. Alexandrou, S. Bacchio, M. Constantinou, J. Finkenrath, K. Hadjiyiannakou, K. Jansen, G. Koutsou, and A. Vaquero Aviles-Casco, Phys. Rev. D **102**, 054517 (2020).

[17] N. Hasan, J. Green, S. Meinel, M. Engelhardt, S. Krieg, J. Negele, A. Pochinsky, and S. Syritsyn, Phys. Rev. D **99**, 114505 (2019).

[18] K. Ottnad, T. Harris, H. Meyer, G. von Hippel, J. Wilhelm, and H. Wittig, Proc. Sci. LATTICE2018 (**2018**) 129 [arXiv: 1809.10638].

[19] N. Yamanaka, S. Hashimoto, T. Kaneko, and H. Ohki (JLQCD Collaboration), Phys. Rev. D **98**, 054516 (2018).

[20] G. S. Bali, S. Collins, B. Glässle, M. Göckeler, J. Najjar, R. H. Rödl, A. Schäfer, R. W. Schiel, W. Söldner, and A. Sternbeck, Phys. Rev. D **91,** 054501 (2015).

[21] K. I. Ishikawa , Y. Kuramashi, S. Sasaki, E. Shintani, and T. Yamazaki (PACS Collaboration), Phys. Rev. D **104,** 074514 (2021).

[22] E. Shintani, K. I. Ishikawa, Y. Kuramashi, S. Sasaki, and T. Yamazaki, Phys. Rev. D **99,** 014510 (2019); **102,** 019902(E) (2020).

[23] K. I. Ishikawa, Y. Kuramashi, S. Sasaki, N. Tsukamoto, A. Ukawa, and T. Yamazaki (PACS Collaboration), Phys. Rev. D **98,** 074510 (2018).

[24] S. Gusken, Nucl. Phys. B, Proc. Suppl. **17,** 361–364 (1990).

[25] S. Sasaki, T. Blum, and S. Ohta, Phys. Rev. D **65,** 074503 (2002).

[26] K. Sasaki and S. Sasaki, Phys. Rev. D **72,** 034502 (2005).

[27] S. Sasaki, K. Orginos, S. Ohta, and T. Blum (RIKEN-BNL-Columbia-KEK Collaboration), Phys. Rev. D **68,** 054509 (2003).

[28] G. Martinelli, C. Pittori, C. T. Sachrajda, M. Testa, and A. Vladikas, Nucl. Phys. **B445,** 81 (1995).

[29] K. I. Ishikawa *et al.* (PACS Collaboration), Proc. Sci. LATTICE2015 (**2016**) 271 [arXiv:1511.08549].

[30] Y. Aoki, Proc. Sci. LAT2009 (**2009**) 012 [arXiv:1005.2339].

[31] Y. Aoki, P. A. Boyle, N. H. Christ, C. Dawson, M. A. Donnellan, T. Izubuchi, A. Juttner, S. Li, R. D. Mawhinney, J. Noaki *et al.*, Phys. Rev. D **78,** 054510 (2008).

[32] C. Sturm, Y. Aoki, N. H. Christ, T. Izubuchi, C. T. C. Sachrajda, and A. Soni, Phys. Rev. D **80,** 014501 (2009).

[33] L. G. Almeida and C. Sturm, Phys. Rev. D **82,** 054017 (2010).

[34] J. A. Gracey, Phys. Lett. B **488,** 175 (2000).

[35] J. A. Gracey, Nucl. Phys. **B662,** 247 (2003).

[36] P. Boucaud, F. de Soto, J. P. Leroy, A. Le Yaouanc, J. Micheli, H. Moutarde, O. Pene, and J. Rodriguez-Quintero, Phys. Lett. B **575,** 256 (2003).

[37] S. Weinberg, Phys. Rev. **118,** 838 (1960).

[38] P. Boucaud, F. de Soto, J. P. Leroy, A. Le Yaouanc, J. Micheli, H. Moutarde, O. Pene, and J. Rodriguez-Quintero, Phys. Rev. D **74,** 034505 (2006).

[39] Y. Iwasaki, arXiv:1111.7054.

[40] K. I. Ishikawa, N. Ishizuka, Y. Kuramashi, Y. Nakamura, Y. Namekawa, E. Shintani, Y. Taniguchi, N. Ukita, T. Yamazaki, and T. Yoshie (PACS Collaboration), Phys. Rev. D **100,** 094502 (2019).

[41] C. Morningstar and M. J. Peardon, Phys. Rev. D **69,** 054501 (2004).

[42] Y. Taniguchi, Proc. Sci. LATTICE2012 (**2012**) 236 [arXiv:1303.0104].

[43] K. I. Ishikawa, N. Ishizuka, Y. Kuramashi, Y. Nakamura, Y. Namekawa, Y. Taniguchi, N. Ukita, T. Yamazaki, and T. Yoshie (PACS Collaboration), Phys. Rev. D **99,** 014504 (2019).

[44] J. Kakazu *et al.* (PACS Collaboration), Phys. Rev. D **101,** 094504 (2020).

[45] E. Shintani, R. Arthur, T. Blum, T. Izubuchi, C. Jung, and C. Lehner, Phys. Rev. D **91,** 114511 (2015).

[46] T. Blum, T. Izubuchi, and E. Shintani, Phys. Rev. D **88,** 094503 (2013).

[47] G. von Hippel, T. D. Rae, E. Shintani, and H. Wittig, Nucl. Phys. **B914,** 138 (2017).

[48] M. Lüscher, Comput. Phys. Commun. **156,** 209–220 (2004).

[49] M. Luscher, J. High Energy Phys. 07 (2007) 081.

[50] G. Martinelli and C. T. Sachrajda, Nucl. Phys. **B316,** 355 (1989).

[51] T. Blum, N. H. Christ, C. Cristian, C. Dawson, G. T. Fleming, G. Liu, R. Mawhinney, A. Soni, P. Vranas, M. Wingate *et al.*, Phys. Rev. D **66,** 014504 (2002).

[52] P. A. Zyla *et al.* (Particle Data Group), Prog. Theor. Exp. Phys. **2020,** 083C01 (2020).

[53] A. Ali Khan *et al.* (*CP*-PACS Collaboration), Phys. Rev. D **65,** 054505 (2002); **67,** 059901(E) (2003).

[54] J. D. Bratt *et al.* (LHPC Collaboration), Phys. Rev. D **82,** 094502 (2010).

[55] R. Tsuji, Y. Aoki, K. I. Ishikawa, Y. Kuramashi, S. Sasaki, E. Shintani, and T. Yamazaki, arXiv:2201.11397.

[56] M. Gorbahn and S. Jager, Phys. Rev. D **82,** 114001 (2010).

[57] T. van Ritbergen, J. A. M. Vermaseren, and S. A. Larin, Phys. Lett. B **400,** 379 (1997).

[58] L. Maiani, G. Martinelli, M. L. Paciello, and B. Taglienti, Nucl. Phys. **B293,** 420 (1987).